

Die approbierte Originalversion dieser Diplom-/
Masterarbeit ist in der Hauptbibliothek der Tech-
nischen Universität Wien aufgestellt und zugänglich.

<http://www.ub.tuwien.ac.at>



The approved original version of this diploma or
master thesis is available at the main library of the
Vienna University of Technology.

<http://www.ub.tuwien.ac.at/eng>

Diplomarbeit

Dosimetric comparison of photon, proton and carbon ion therapy for meningioma patients

am
Atominstitut
Technische Universität Wien

und der
Abteilung für Radioonkologie
Universitätsklinik für Strahlentherapie
Medizinische Universität Wien

betreut von
Ao. Prof. Dipl.-Ing. Dr. Dietmar Georg
Mag. Barbara Knäusl, Ph.D.

von
Lukas Sölkner, B.Sc.
Glatzgasse 4/24
1190 Wien

16.September 2013

Danksagung

Zuallererst möchte ich mich bei Ao.Univ.Prof. Dipl.-Ing. Dr.techn. Dietmar Georg für die Unterstützung bedanken. Durch seine Motivation und seinen Einsatz ist diese Arbeit erst möglich geworden.

Bedanken möchte ich mich ganz besonders bei Mag. Barbara Knäusl, Ph.D., die mir im Laufe dieser Arbeit mit viel Geduld und vielen guten Ratschlägen zur Seite stand.

In diesem Zusammenhang sei auch Dipl.-Ing. Wolfgang Lechner, Mag. Peter Kuess und Anton Watzinger, B.Sc. gedankt, die stets ein offenes Ohr für Fragen hatten.

Ein Dank sei auch Ass.Prof. Dipl.-Ing. Dr.techn. Karin Poljanc ausgesprochen, die mich ins AKH vermittelt hat und mir in administrativen Angelegenheiten Rückhalt gab.

Im Speziellen möchte ich meinen Eltern und meiner Schwester danken, die mich stets unterstützen, an mich glauben und mich immer liebevoll aufnehmen.

Ich möchte mich des Weiteren bei Dipl.-Ing. Ronald Sladky, Ph.D. bedanken, den ich nach jedem Gespräch bereichert verlasse und durch den ich stets neue Facetten weit über die Wissenschaft hinaus entdecken darf. Ein besonderer Dank gilt Cristina, die mich von Spanien aus inspiriert und mir auch in schweren Zeiten ein Lächeln schenkt.

Abstract

Purpose: To compare various modalities of radiotherapy for the treatment of atypical meningioma.

Methods: The delineation of two target volumes ($PTV_{initial}$ and PTV_{Boost}) was done for ten patients. Intensity-modulated radiation treatment plans with prescribed doses of 50 Gy(RBE) and 18 Gy(RBE) were generated for photons (IMXT), protons (IMPT) and carbon ions (^{12}C), respectively. For light ion beam treatments, a horizontal fixed beam line without gantry was assumed. The following treatment modality combinations were compared:

- IMXT (initial) + IMXT/IMPT/ ^{12}C (Boost),
- IMPT (initial) + IMPT/ ^{12}C (Boost),
- ^{12}C (initial) + ^{12}C (Boost).

Treatment plan quality was analyzed and compared on the basis of dosimetric parameters, such as conformity index, homogeneity index, and various dose-volume parameters.

Results: Results revealed that sole light ion modalities are the better alternative, considering the reduced integral dose and the higher degrees of homogeneity and conformity, when compared to photon therapy.

IMPT and ^{12}C exhibited similar characteristics, with ^{12}C leading to a sharper penumbra around the target volume and reduced integral dose.

The light ion treatment modalities demonstrated better sparing of the organs at risk, due to the reduced high-dose areas. Particularly with respect to brainstem, eyes and cerebellum, the dose burden was reduced to a minimum and the dose parameters differed significantly from those of the photon therapy.

Conclusion: Even though a fixed horizontal beam with protons and carbon ions was used, various improvements were achieved as compared to the IMXT: higher levels of

conformity and homogeneity of the target volumes, and a better sparing of the organs at risk.

Kurzzusammenfassung

Ziel: Ziel dieser Diplomarbeit war der Vergleich verschiedenen Bestrahlungsmodalitäten für atypische Meningiome.

Methoden: Bei 10 Patienten wurden jeweils zwei Zielvolumina ($PTV_{initial}$ und PTV_{Boost}) eingezeichnet. Intensitätsmodulierte Bestrahlungspläne mit einer vorgeschriebenen Dosis von 50 Gy(RBE) beziehungsweise 18 Gy(RBE) wurden für Photonen (IMXT), Protonen (IMPT) und Kohlenstoffionen (^{12}C) mit Hilfe unterschiedlicher Bestrahlungsplanungsprogramme erstellt. Für die Protonen und Kohlenstoffionen wurde ausschließlich eine horizontale Strahlaustrittsrichtung ohne Gantry angenommen.

Es wurden folgende Kombinationen aus den unterschiedlichen Modalitäten erstellt:

- IMXT (initial) + IMXT/IMPT/ ^{12}C (Boost),
- IMPT (initial) + IMPT/ ^{12}C (Boost),
- ^{12}C (initial) + ^{12}C (Boost).

Die Qualität der Pläne wurde anhand dosimetrischer Parameter wie des Konformitätsindex, des Homogenitätsindex und diverser Dosis-Volumen Parameter wie der maximalen und der mittleren Dosisbelastung analysiert und verglichen.

Resultate: Als Ergebnis dieser Studie lässt sich zusammenfassen, dass eine Bestrahlung mit ausschließlich Leichtionen der Photonentherapie hinsichtlich der reduzierten integralen Dosis, der höheren Homogenität sowie der höheren Konformität überlegen war.

IMPT und ^{12}C wiesen ähnliche Charakteristika auf, wobei mit ^{12}C ein steilerer Dosisgradient um das Zielvolumen und eine reduzierte integrale Dosis erreicht wurde.

Hinsichtlich der Risikoorgane zeigten die Leichtionentherapien eine bessere Schonung durch einen reduzierten Hochdosisbereich. Besonders bei beiden Augen, dem Hirnstamm und dem Kleinhirn fiel die Dosisbelastung im Vergleich zur Photonentherapie in Niedrigdosisbereiche ab und die Dosisparameter unterschieden sich signifikant.

Konklusion: Verglichen mit IMXT konnten trotz der Verwendung eines horizontalen Strahles mit Protonen und Kohlenstoffionen Verbesserungen hinsichtlich der Konformität und der Homogenität der Zielvolumen und eine bessere Schonung der Risikoorgane erreicht werden.

Contents

Danksagung	iii
Abstract	v
Kurzzusammenfassung	vii
Introduction	5
1 Basics of radiation therapy	9
1.1 Radiation physics	9
1.1.1 Interaction processes of photons	10
1.1.1.1 Coherent scattering	11
1.1.1.2 Photoelectric effect	12
1.1.1.3 Compton effect	15
1.1.1.4 Pair production	16
1.1.1.5 Relative importance of the various processes	17
1.1.2 Interaction of charged particles	18
1.1.2.1 Stopping power	19
1.1.2.2 Linear energy transfer (LET)	20
1.1.2.3 Relative biological effectiveness (RBE)	21
1.1.2.4 Comparison of protons and heavier ions	22
1.2 Volume concepts	23
1.2.1 Volume concepts in radiation oncology	24
1.2.2 Dose-volume histogram (DVH)	26
1.3 Delivering systems in radiation therapy	27
1.3.1 Linear accelerator (LINAC)	27
1.3.2 Pre-accelerators for light ions	28
1.3.3 Cyclotron	28
1.3.4 Synchrotron	30
1.4 Passive scattering and active scanning	31
1.4.1 Passive scattering	31
1.4.2 Active scanning	32
1.5 Dose calculation algorithms	32
1.5.1 Correction-based algorithms	33
1.5.2 Model-based algorithms	33
1.5.3 Pencil beam algorithm	34
1.5.4 Monte Carlo algorithm	36
1.6 Treatment techniques	37

1.6.1	Conformal radiotherapy (CRT)	38
1.6.2	Intensity modulated X-ray therapy (IMXT)	39
1.6.3	Single-field uniform dose (SFUD)	40
1.6.4	Intensity modulated proton therapy (IMPT)	40
2	Patients and methods	41
2.1	Medical aspects	41
2.1.1	Meningioma	41
2.2	Patients	42
2.2.1	Target volumes	42
2.2.2	Organs at risk (OAR)	43
2.3	Treatment planning systems	45
2.3.1	Monaco	46
2.3.1.1	Cost functions	46
	Target-EUD:	47
	Quadratic overdose:	48
	Serial cost function:	48
	Parallel cost function:	49
2.3.1.2	Treatment plan configuration	49
2.3.2	XiO	51
2.3.2.1	Treatment plan configuration	51
2.3.3	TRiP	53
2.3.3.1	Treatment plan configuration	54
2.4	CERR	55
2.5	Evaluation parameters	56
2.5.1	DVH Export	57
2.5.2	Dosimetric parameters	57
2.5.2.1	Dose-volume-parameters	57
	Code for the function to calculate dose at volumes	57
2.5.2.2	Mean dose	59
2.5.2.3	Homogeneity index	60
2.5.2.4	Conformity index	60
2.5.3	Statistical evaluation	60
2.5.3.1	Mean value and standard deviation	60
2.5.3.2	Student's t-test	61
2.5.4	Operating instructions for the evaluation software	61
3	Results	63
3.1	Target volumes	63
3.1.1	Initial and boost plans	63
3.1.2	Combined plans	67
3.2	Organs at risk (OAR)	68
3.2.1	Primary OAR	68
3.2.1.1	Eyes	68
3.2.1.2	Optical pathway	70
3.2.1.3	Brainstem and cerebellum	72
3.2.1.4	Pituitary gland	73

3.2.1.5	Comparison of mixed modalities for selected primary OAR	74
3.2.2	Secondary OAR	75
3.2.2.1	Brain hemisphere	75
3.2.2.2	Secondary contralateral OAR	76
3.2.2.3	Secondary ipsilateral OAR	77
4	Summary and Outlook	79
5	Appendix	83
	Bibliography	87
	Abbildungsverzeichnis	95

Introduction

History of photon therapy

The discovery of X-rays by K.W. Roentgen in the year 1895 represents the birth of radiotherapy (RT) [1]. X-rays are a form of electromagnetic radiation with a wavelength in a range of 0.01 to 10 nm, corresponding to photon energies in the range of 100 eV to 100 keV ([2],p.11). Already in those early days of radiation physics, scientists endeavored the utilization of the discovered radiation for medical purposes. For example, skin lesions were treated with the aid of X-rays. Due to the lack of physical and biological knowledge, however, the first attempts were barely successful.

In the course of the following decade, the fundamentals of subatomic and electromagnetic particles were discovered. Soon after Roentgen's milestone H. Becquerel reported about the phenomenon of radioactivity [3], and P. and M. Curie discovered radium [4]. In the year 1896, the first successful treatment with X-rays was already performed by L. Freund in Vienna [5]. A five year old girl suffering from hairy moles covering her whole back was treated. However, resulting from the lack of knowledge regarding the interaction of radiation and biological tissue cancer control was neglected and the lethal rate was high [6]. In 1901, H. Becquerel and P. Curie published a paper about physiologic effects caused by radium radiation [7], which inspired scientists to consider medical treatments for various diseases. In the year 1904, one of the first RT reports about the medical applications of X-rays and radium, the so-called Curie-therapy, were available [8, 9].

During the first three decades of the 20th century physicists and biologists tried to gather information about the correlation between time and dose on cell survival in terms of radiation therapy. Around 1930, C. Regaud [10] and H. Coutard [11] discovered that less exposure to radiation resulted in cell recovery. Furthermore, they found that healthy tissue cells are able to recover better from radiation injuries than cancerous tissue cells. For the first time, they considered fractionated therapy in which the total radiation dose is delivered in parts, in order to minimize the negative reaction and side effects on the healthy tissue.

The development of the first super-voltage X-ray tubes provided the basis for linear accelerators for photon radiation, in the late 1920's [12]. The linear accelerators were grounded on the principle of applying a dynamic electromagnetic field. From the 1950's on, cobalt teletherapy machines and megavoltage linear accelerators were developed. The first linear accelerators for clinical purposes became available around 1955, but were put to widespread use in the 1960's and 1970's [13].

In the past decades, technological progress depended on the improvement of computer and imaging techniques which nowadays realize three-dimensional based treatment planning for radiotherapy. Computer Tomography (CT)- and Magnetic Resonance (MR)- scans are necessary and indispensable for a good differentiation of tumor volume from healthy surrounding organs in the process of radiotherapy treatment planning ([14],chapter 31).

In order to achieve high doses around the tumor volume and to avoid high exposure of normal tissue to radiation, conformal radiation therapy (CRT) was proposed performing geometrical field shaping ([14],chapter 43). Nowadays, beside CRT Intensity-Modulated radiotherapy (IMXT), based on the principle of inverse dose optimisation, is a widely used radiotherapy technique, which had been described for the first time in the year 1978. In the mid 1990's it was applied in practice, following improvements and developments of the computer equipment [15].

History of light ion therapy

In the beginning of the 20th century, when the first therapy forms with X-rays were established, E. Rutherford [16] used X-rays and radiation of radioactive atoms to initiate electrical conduction in gases and discovered two types of emission: the alpha rays and the beta rays. In 1911, Rutherford postulated the nuclear model of the atom which was later adapted by N. Bohr. In 1919 Rutherford performed an experiment in which alpha particles were shot at nitrogen atoms to demonstrate that ejected particles occurred which appeared to be the nuclei of hydrogen. Rutherford named these positively charged particles "protons".

In the 1930's, E.O. Lawrence developed the first cyclotron for protons [17]. The cyclotrons were based on the principle of applying a potential difference like linear accelerators and provided the basis for the first particle accelerators [18, 19, 20]. Furthermore, two milestones in the 1940s were the establishment of the first electron beam therapy by means of a betatron and the invention of the synchrotron [21] which enables phase stability for reaching high energy levels without any need of enlarging the device as with

cyclotrons ([22],p.161,[23],p.61). However, the concept of phase stability became the basis for electron and high energy proton accelerators thereafter ([24],p.334f).

In the year 1946, Robert R. Wilson, the founding director of Fermi National Labs, suggested that the dose distribution characteristics of light ion beams, like proton beams, might be an attractive option for the radiation therapy of cancer [25].

One of the most crucial difference between photons and light ions is their depth dose characteristics (Figure 1). When photons interact with biological tissue, stochastic events like absorption processes and scattering processes occur. Consequently, the photon beam spreads rapidly after entering the tissue and has no defined range. Correspondingly, the absorption curve of the photon beam reveals an initial build up area followed by an exponentially dose decrease ([24],p.46f).

Contrary to the photon beam, light ion beams do have a finite range and less scattering due to their mass. The interaction probability and so the probability of ionization increase with the loss of the particle's velocity through the tissue. The dose maximum, the so called Bragg peak, occurs at a depth proportional to the initial energy of the particles [25, 26, 27, 28] (Figure 1).

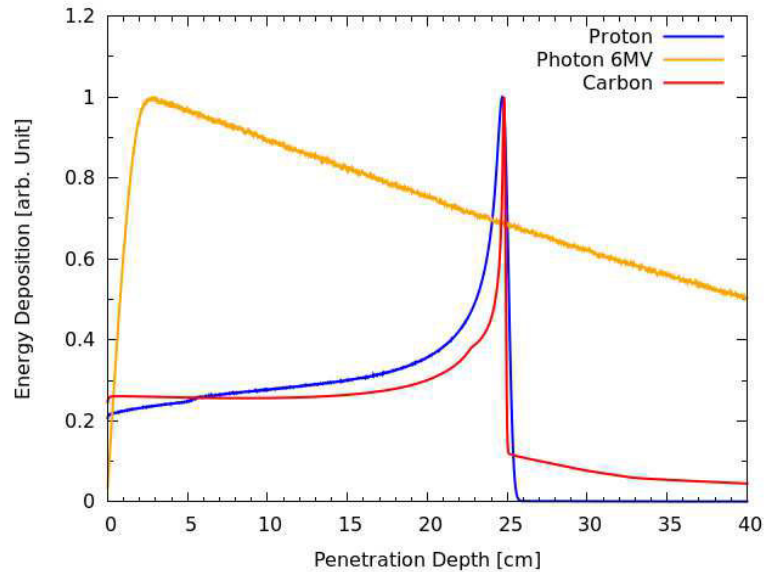


FIGURE 1: Comparison of the depth dose distribution of photons, protons and carbon ions as a function of the penetration depth

About ten years after the suggestions by Wilson, the Lawrence Berkeley Laboratory performed initial clinical studies on patients [29] and the Gustav Werner Institute in Sweden began with proton treatment research [30]. The first hospital-based proton facility was built at the Loma Linda University Medical Center (LLUMC) in the USA in the 1970's [31].

Since the 1950's also radiation treatment with ions heavier than protons were of interest and several studies were initiated. From the late 1950's up to the early 1990's the Lawrence Berkley Laboratory for example treated 2054 patients with helium ions [32]. Moreover, between 1975 and 1992, 433 patients have been treated with ions like neon, argon or carbon [33]. Currently, radiation therapy with carbon ions is performed in Europe at Centro Nazionale di Adroterapia Oncologica (CNAO) in Italy and at Heidelberg Ionenstrahl-Therapiezentrum (HIT) in Germany ([24],p.688f). Another therapy center, called MedAustron, is built at Wiener Neustadt in Austria and the first patient treatment is planned for 2015.

The aim of this master thesis is to analyse the characteristics of modern X-ray, proton and carbon ion therapy forms and to compare and highlight specific benefits and advantages of these three treatment methods by means of skull based meningioma patients.

Chapter 1

Basics of radiation therapy

1.1 Radiation physics

The photon radiation used in medicine encompasses a range from low energetic X-rays (10 keV) to high energetic X-rays (18 MeV) produced by X-ray tubes and accelerators as well as the emitted γ or β^- radiation of radioactive nuclei with energy ranges from keV to several MeV. The produced irradiation can have a continuous spectrum, the bremsstrahlung spectrum, or a characteristic spectrum in the case of radioactive nuclei. Interaction of photon radiation with matter can cause fully or partly absorption of the photon energy or a change of the photon direction, the so called scattering. These kind of interactions can lead to the production of free charged secondary particles like electrons or positrons or photons. The secondary particles for their part can excite and ionize the surrounding tissue, depose energy and evoke biological effects. Since the ionization is mainly caused indirectly by the secondary particles the photon radiation is regarded as indirect ionizing type of radiation.

The interaction of light ions like protons or carbon ions with matter depends on the velocity corresponding to the kinetic energy, the charge as well as the mass of the particles. Another important parameter is the perpendicular distance between the charged particle direction before the interaction and the atomic nucleus. Light ions are able to excite and ionize the surrounding matter by transferring their energy in a direct way. The physical quantity for the description of the energy losses of heavy charged particles due to interaction with matter are the collision stopping power and the radiation stopping power. The density of energy lost by the traveling of charged ionizing particles through the matter is called linear energy transfer (LET) and the amount of produced electrical charges due to the interaction is called ionization density.

1.1.1 Interaction processes of photons

For the description of the interaction processes of photon beams with matter three different steps have to be distinguished. The primary interaction process causes attenuation of the initial photon beam, a loss of intensity:

$$I = I_0 \cdot e^{-\mu d} \quad (1.1)$$

The attenuation is described as the relation of the intensity after transmission through the absorbing matter I with a thickness d to the initial intensity I_0 .

The linear attenuation coefficient μ [1/cm] is related to the atomic mass A and the density ρ of the material as well as the Avogadro constant N_A and the atomic cross section σ :

$$\mu = \frac{N_A}{A} \cdot \rho \cdot \sigma \quad (1.2)$$

Since μ and ρ are approximately linear it is possible to consider a mass attenuation coefficient μ/ρ [cm²/g]. In this way the mass attenuation coefficient is independent of the density.

The second interaction step of photons with matter is the transformation of photon energy into kinetic energy E_{kin} corresponding to the energy transfer from photons to charged secondary particles. This process can be described with the physical quantity called Kerma (Kinetic energy released per unit mass) which represents the kinetic energy of all secondary charged particles liberated by uncharged photons in matter with mass m . Kerma K is defined by:

$$K = \frac{dE_{kin}}{dm} \quad (1.3)$$

The third step is represented by the energy absorption E within the matter arising from the kinetic energy of the secondary particles and is a measure of the energy dose D [Gy].

$$D = \frac{dE}{dm} \quad (1.4)$$

However, the phenomenon of attenuation arises from four major types of interaction which are based on one of the three steps:

Coherent scattering σ_{coh}

Photoelectric effect τ

Compton effect σ_c

Pair production π

Each of them is represented by its own attenuation coefficient which is related to the photon energy and the atomic mass of the absorbing matter. The linear attenuation coefficient μ is the sum of them:

$$\frac{\mu}{\rho} = \frac{\sigma_{coh}}{\rho} + \frac{\tau}{\rho} + \frac{\sigma_c}{\rho} + \frac{\pi}{\rho} \quad (1.5)$$

Interaction processes with the electrons in the atomic shell are the coherent scattering, the photo effect and the Compton effect. The pair production arises from the interaction of the photon with the electromagnetic field of an atomic nucleus.

1.1.1.1 Coherent scattering

Coherent scattering, also called Rayleigh scattering or classical scattering, occurs in materials with a high atomic number and with photons of a low energy level. The incoming photon interacts with the electrons in the atomic shell, causes electron oscillation and gets scattered. The frequency of the scattered photon and the oscillating electron are equal. The electrons act like a sender and emit the absorbed energy completely again without absorption. Hence, the incident photon and the scattered photon have the same energy without any losses and the same phases. (Figure 1.1) The atomic shell remains unchanged.

The classical scattering coefficient σ_{coh} decreases above 10 keV with the square of the photon energy and increases with $Z^{2.5}/A$ and the density ρ , whereby Z is the atomic number and A is the mass number:

$$\sigma_{coh} \propto \rho \frac{Z^{2.5}}{A} \quad (1.6)$$

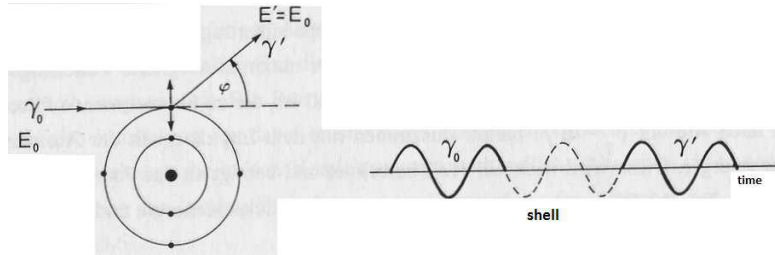


FIGURE 1.1: Coherent scattering ([2],p.120)

This effect is not relevant in radiation therapy because the dose related to the low energy level of the photons would not cause any destruction of irradiated tissue.

1.1.1.2 Photoelectric effect

In the photoelectric effect an incident photon is completely absorbed after the interaction with an orbital electron of an atom. The entire energy of the photon is transferred to the electron. The difference between the photon energy and the binding energy of the electron (which depends on the atomic number) corresponds with the kinetic energy of the electron getting ejected if $E_y > E_b$.

$$E_{kin} = E_y - E_b \quad (1.7)$$

The process is shown in Figure 1.4.

The probability of the photoelectric effect is given by the photo absorption coefficient τ . It increases with the density ρ and Z^{4-5}/A and is therefore likeliest for heavy absorbers with high atomic numbers.

Photo absorption is most probable if the energy of the photon and the electron shell are equal. Consequently, the photo absorption coefficient, which is energy dependent, reaches a maximum at an energy of the inner electron shell (K-shell), falls off rapidly after deceeding this energy level and increases again to the next energy level of the next electron shell (L-shell). This discontinuities are called absorption edges and are shown in Figure 1.2.

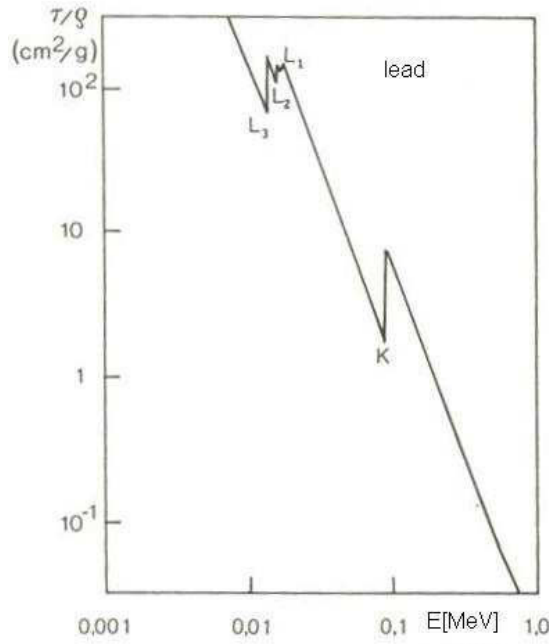


FIGURE 1.2: Absorption Edges([2],p.108)

The photo absorption coefficient dependencies are given by:

$$\tau \propto \rho \frac{Z^{n+1}}{A} E^{-3} \quad (1.8)$$

The energy exponent n is for light elements $n=3.6$ and for elements with high atomic numbers $n=3$.

The ejected photoelectrons have an angular distribution which is energy dependent. Low photon energies cause an almost perpendicular ejection of the photoelectrons relative to the incident photon beam direction at the area of interaction. The higher the photon energy is, the smaller the emission angle becomes and tends to the forward direction [2],p.109) (Figure 1.3).

After the photon electron is ejected as secondary particle, the inner atomic shell contains a vacancy. As a consequence of energetic reasons, the vacancy can be filled by an electron from outer atomic shells under emission of characteristic X-rays, a tertiary radiation (Figure 1.4). The energy of the characteristic X-rays corresponds to the binding energy differences of the electron states in the shells. Furthermore, the characteristic X-rays can cause the ejection of a monoenergetic electron, also known as Auger electron, if they are absorbed by another electron of the atom and exceed its binding energy. The Auger

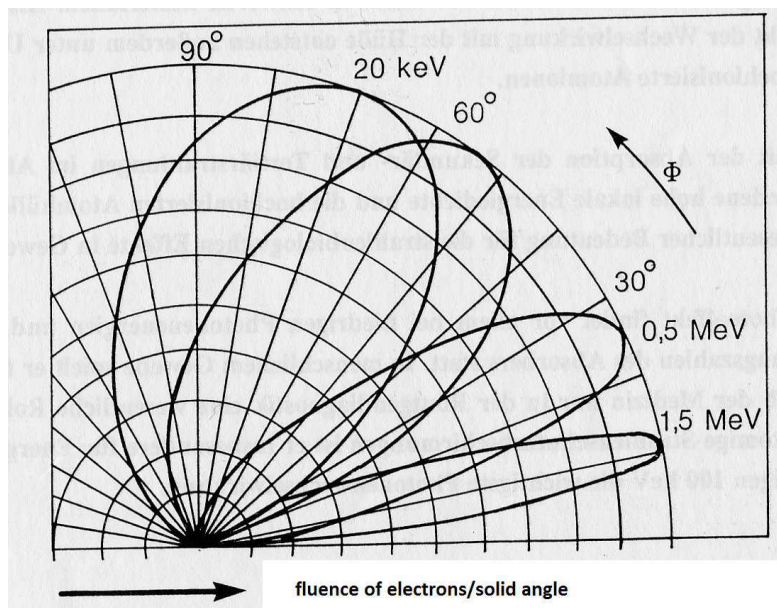


FIGURE 1.3: Emission of electrons([2],p.109)

effect can be understood as internal photoelectric effect due to the interaction of the characteristic X-rays with another electron of the same atom.

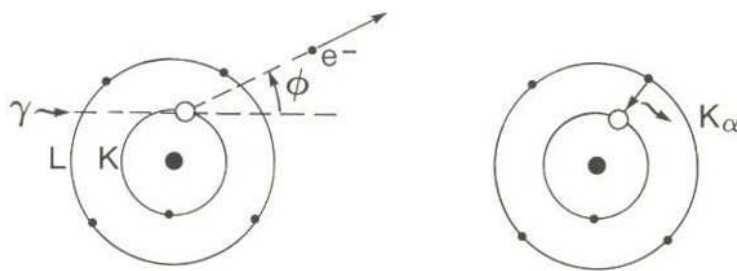


FIGURE 1.4: Photoelectric effect ([2],p.107)

If the probability of emission of a characteristic X-ray is called the fluorescence yield ω and the Auger yield α then the total probability is 100 percent.

$$\omega + \alpha = 1 \quad (1.9)$$

α does not depend on Z , ω has a dependency of Z^4 .

1.1.1.3 Compton effect

The Compton effect, an incoherent scattering process, is the interaction of a photon with a weak bounded (quasi free) electron in an outer shell of an atom. The binding energy is much weaker than the photon energy, in contrast to the photoelectric effect, which becomes probable when the energy of the photon is equal or slightly higher than the binding energy. The incident photon transfers parts of its energy and momentum to the electron of the outer shell. The photon is scattered at an angle ϕ and the electron is ejected out of the atomic shell at an angle Φ relative to the direction of the incident photon leading to an ionization of the atomic shell (Figure 1.5). The transferred energy and the scattering angle depend on the photon energy. At very low incident photon energies the scattered photons are almost symmetrically distributed perpendicular to the incident photon direction and even backscattering is possible. The higher the photon energy is, the more scattering occurs in the forward direction (Figure 1.6).

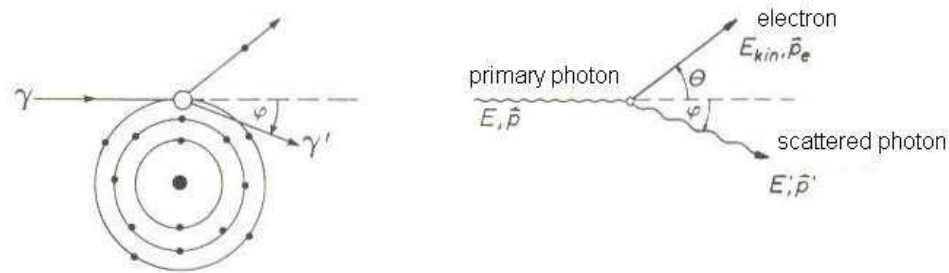


FIGURE 1.5: Compton effect ([2],p.112)

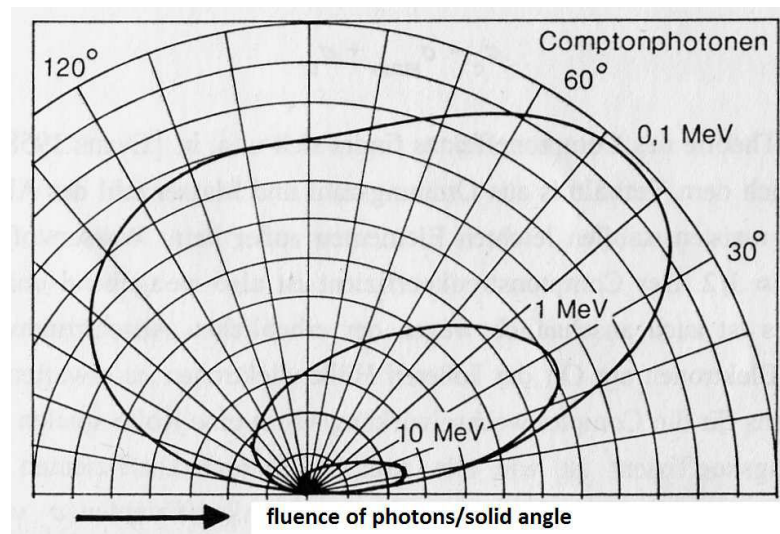


FIGURE 1.6: Compton photon ([2],p.112)

The probability that a Compton effect occurs is given by the Compton attenuation coefficient σ_c which is the sum of the Compton scattering coefficient and the Compton energy transfer coefficient.

$$\sigma_c = \sigma_{scatter} + \sigma_{tr} \quad (1.10)$$

The Compton attenuation coefficient σ_c is proportional to Z/A of the absorber. For most of the stable, light elements (except hydrogen) the atomic number Z is about the neutron number N so that Z/A is about $1/2$. That means that the Compton attenuation coefficient is almost independent of the atomic number as the nuclear force is mainly shielded by the inner electrons. Furthermore, the Compton attenuation coefficient is proportional to the density and the photon energy, which ranges from 0.2 MeV to 10 MeV for the most materials (Formula 1.11)

$$\frac{\sigma_c}{\rho} \propto E^{-1/2} \quad (1.11)$$

The Compton electron ejection takes place as a result of the momentum conservation in the forward direction. The scattering angles ranges from 0 to 90 degree.

The photon's energy after the collision with the electron can be analyzed by the laws of conservation of energy and momentum. The energy of the scattered photon $h\nu'$ is demonstrated in equation 1.12. m_e corresponds to the mass of the electron.

$$h \cdot \nu' = \frac{h \cdot \nu}{1 + \frac{h \cdot \nu}{m_e \cdot c^2} \cdot (1 - \cos(\phi))} \quad (1.12)$$

1.1.1.4 Pair production

Photons can be described as electromagnetic energy packets. Thus they are able to interact with the electrical field of charged particles like the protons in the atomic nucleus. If the photon's energy exceeds a threshold of 1.022 MeV, it can be completely absorbed in the Coulomb field of an atomic nucleus and form an electron-positron pair which tends to be emitted in the forward direction relative to the incident photon.

The energy of the photon E_γ is partly transferred to the rest mass m_0 of the particle-antiparticle pair and to the kinetic energy E_{kin} of both the electron and the positron (Formula 1.13)

$$E_{kin} = E_\gamma - 2m_0c^2 = E_\gamma - 1.022MeV \quad (1.13)$$

The probability of pair production increases with the logarithm of the photon's energy, the density of the absorbing material and with Z^2/A . The pair production dependence is expressed in the equation 1.14 if $E_\gamma > 1.022 \text{ MeV}$.

$$\pi \propto \rho \frac{Z^2}{A} \log(E_\gamma) \quad (1.14)$$

If a slow moving positron, also known as thermal positron with the same energy like an electron, combines later on with an electron, they produce so called annihilation radiation consisting of two photons with 511keV each. Because of the conservation of momentum the two photons are ejected in opposite directions. This process is also called inverse pair production.

1.1.1.5 Relative importance of the various processes

As shown in the previous sections the mass attenuation coefficients of the various interactions depend on the atomic number and the energy of the photon in different ways. The density-dependencies are constant. These are summarized in Table 1.1.

The most important absorber in medicine is human tissue, which is nearly equivalent to water, with an effective atomic number of 7 to 8. The medically used photon energy in radiation therapy ranges from 6 MeV - 18 MeV and for imaging purposes about several keV. The kind of interaction process is influenced by the energy of the photon and the atomic mass of the irradiated material. Furthermore, the respective process is responsible for the current attenuation, the energy transfer and the absorption of the photon radiation.

The photoelectric effect prevails for heavy elements up to a photon energy of 1 MeV. For the medical field, except for X-ray diagnostic, this effect is almost negligible because of the smaller photon energies.

Interaction	$f(Z,A)$	$f(E_\gamma)$	$f(\text{Density})$	Secondary radiation
Coherent scattering	$Z^{2.5}/A$	E_γ^{-2}	ρ	-
Photoelectric effect	Z^4/A	E_γ^{-3}	ρ	electron, X-ray, Auger-electron
Compton effect	Z/A	$E_\gamma^{-0.5}$	ρ	electron
Pair production	Z^2/A	$\log(E_\gamma)$, if $E_\gamma > 1022\text{keV}$	ρ	electron, positron

TABLE 1.1: Dependencies of various interaction processes

The Compton effect is the dominant interaction process for a broad range of photon energies and low atomic numbers (up to about $Z=10$) and plays the major role for therapeutic and diagnostic photon radiation from 30 keV on. For human tissue with atomic numbers of 7 to 8 the Compton effect is the predominant interaction process.

The pair production becomes more important for materials with low atomic number from 10-20MeV on. For heavy absorbers with $Z > 20$ the pair production is the most important interaction process above 10MeV.

Figure 1.7 shows at a glance in which ranges the interaction processes are dominant. The lower pointed area depicts the relevant part of the diagram for human tissue.

More detailed informations of the interactions processes of photons can be found in “The Handbook of Radiotherapy Physics” ([14],chapter 4), “The Physics of Radiation Therapy” ([34],chapter 2.7, 3.4, 5) and in “Strahlenphysik, Dosimetrie und Strahlenschutz, Band 1” ([2],chapter 4).

1.1.2 Interaction of charged particles

This chapter gives an overview about the interaction of charged particles and is based on “Ion beam therapy” ([24], chapter 4) and in “Strahlenphysik, Dosimetrie und Strahlenschutz, Band 1” ([2], chapter 6).

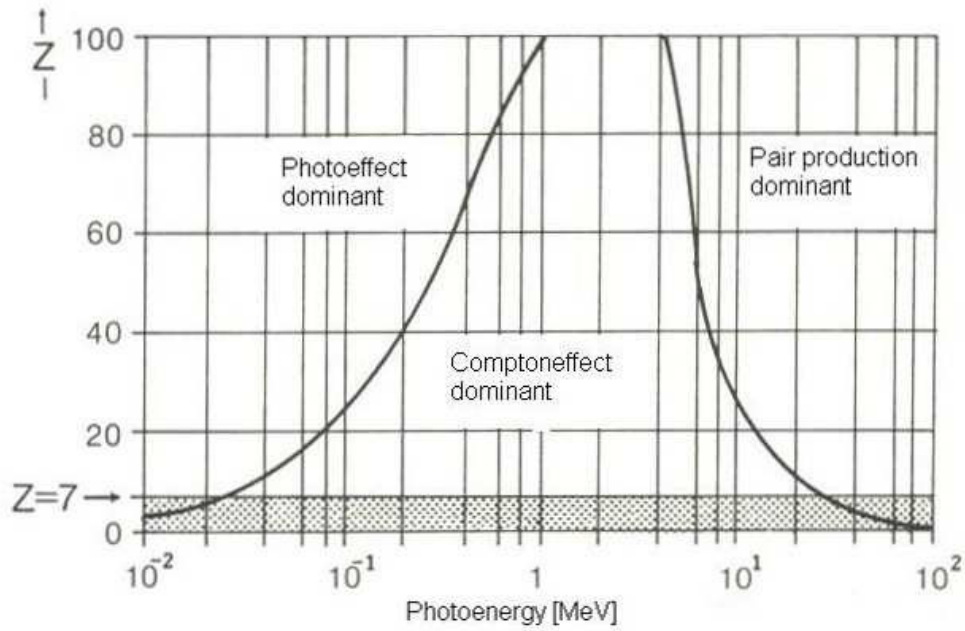


FIGURE 1.7: Ranges of dominance of various interaction processes ([2],p.125)

Contrary to photons, charged particles like protons and other ions are directly ionizing and have a reduced deflection while passing tissue caused by their higher mass. One of the most significant differences is the absorption curve of charged particles in matter. It shows a slight initial increase along higher penetration depth and a steep rise and fall-off toward the end of the particle's range. This is shown in Figure 1.8 and in Figure 1 in the introduction.

1.1.2.1 Stopping power

While the charged particles traverse the biological tissue they interact mainly via Coulomb forces with the electrons of the target tissue. Thus, excitation and ionization of the atoms along the trajectory are occurring and the charged particles loose energy to the surrounding tissue along their track. The energy losses per unit path length, also known as stopping power S_{col} , can be described by the formula 1.15.

$$S_{col} = \frac{dE}{dx_{col}} \approx \rho \frac{Z (z * e)^2}{A v^2} \quad (1.15)$$

The stopping power S_{col} is a form of material property which describes the energy absorption by matter. It depends on the density ρ and the ratio Z/A of the target

material, as well as the charge z and the velocity v of the incident particle and the elementary charge e .

For non-relativistic particle-energies S_{col} is indirect proportional to the square of the velocity of the particle. This leads to an quadratic increase of the energy losses per unit path length. Thus, the energy losses increase with slower velocities, at very slow velocities the increase is even logarithmically. This fact is the reason the steep rise and fall-off at the end of a particle's range, also called Bragg peak. In other words the energy losses corresponding to the relative dose is a function of the penetration depth. This is shown in Figure 1.8.

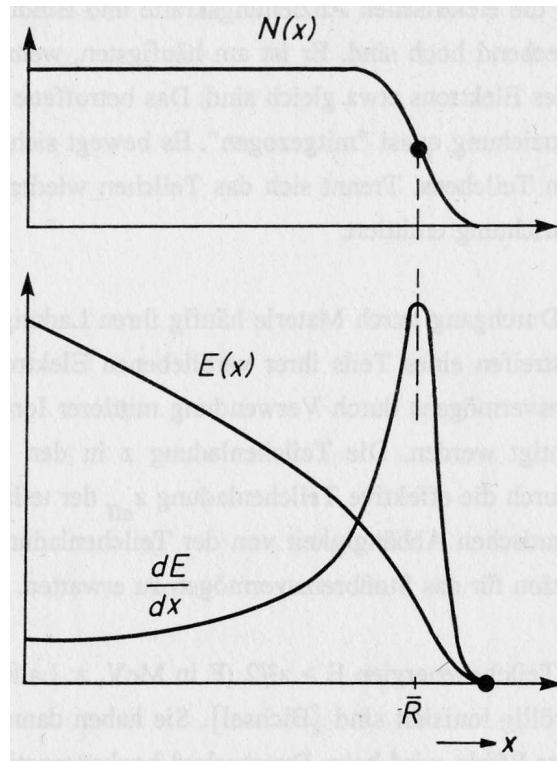


FIGURE 1.8: Energy losses and amount of particles N as a function of the penetration depth([2],p.191)

Furthermore, S_{col} increases according to 1.15 quadratically with the charge and does not depend on the mass of the particle.

1.1.2.2 Linear energy transfer (LET)

In this context also the linear energy transfer (LET) is an important quantity. Different from the stopping power the LET describes the energy deposit of an ionizing particle itself while traversing matter. A distinction has to be drawn between restricted and unrestricted LET. The restricted LET takes only secondary electrons up to a certain

energy limit into account. The aim is to focus upon the energy transferred in the vicinity of the primary particle track and to exclude higher energetic secondary electrons, so called delta electrons. These delta electrons are capable to ionize matter by themselves. The unrestricted LET takes every produced secondary electron by the ionizing particles into account and is numerically equal to the stopping power.

However, the LET is not a constant value. It depends on the charge and the energy of the projectile ion as well and thus the depth dependencies of the LET reveals a Bragg maximum. Furthermore, the LET varies with the ion species. If ions traverse the same matter with the same velocity, the dose density and the number of produced secondary electrons does not need to be necessarily identical. According to the formula 1.15, the deposit dose increases among others with the square of the effective charge of the projectile ions.

1.1.2.3 Relative biological effectiveness (RBE)

The relative biological effectiveness (RBE) is a quantity that describes the biological impact of different types of radiation. As demonstrated in Figure 1.9 beams of various qualities can cause different biological effects.

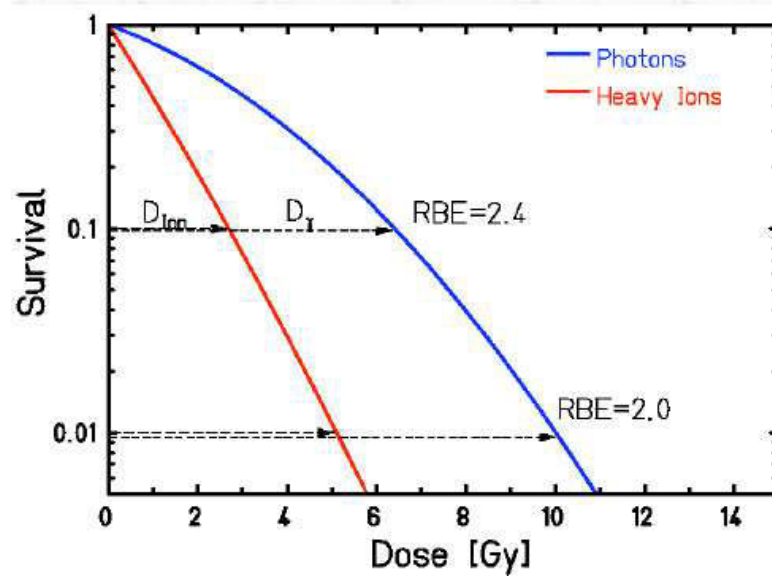


FIGURE 1.9: Relative biological effectiveness for carbon ions and protons [35]

The RBE is defined by the ratio of the energy dose of a reference radiation and the energy dose of a comparative radiation for the same biological impact. As reference radiation mostly 250 kV X-rays with a low LET or γ -radiation of ^{60}Co is used.

For therapeutic purposes the RBE of photons is considered as 1 and of protons as 1.1 [36], even if early investigations showed, that the RBE of protons is dependent on the energy. The RBE of carbon ions is more complex and varies with tissue density and energy [37].

RBE is even partly related to the LET. The increased stopping power towards the end of the ion's range at the Bragg peak corresponds to more biological damage and thus to a higher RBE. The rise of RBE and LET leads up to 100-200 keV/ μm .

Additionally, the RBE value does also depend on the oxygen environment, the dose rate, the cell type and the observed biological effect. As a consequence of that, the RBE also varies with the experimental conditions. These has to be taken into account for the determination of the RBE of a specific radiation.

Furthermore, the magnitude RBE-values are important parameters for therapeutic purposes. Carbon ions reveal an more elevated RBE in the tumor compared to the surrounding tissue as photons and protons, which increases the biological impact in terms of malignant cell death [36, 37].

1.1.2.4 Comparison of protons and heavier ions

When mono-energetic ion beams traverse the same distances in matter the number of collisions are depending on the ion species. A different number of collisions causes diverse ranges. This is called "straggling". The straggling of protons in biological tissue is about 1 percent. The heavier the ion is, the less straggling occurs. Helium for example shows only 50 percent of the proton's straggling. This fact results from the higher amount of mass which avoids high deflection after the collision with other particles and thus reduces straggling (Figure 1.10).

From the clinical point of view this reduced straggling of heavier ions enables higher precision for the treatment and improved organ at risk sparing in the vicinity of the target volume. Consequently, decreased lateral scattering and a sharper Bragg peak can be observed for heavier ions when compared to protons (Figure 1.11).

On the other hand, heavier ions reveal a fragmentation tail of lighter fragment particles after the collision with other particle. Thus a tailing of the Bragg peak occurs which causes a low dose level in higher penetration depths (Figure 1.11).

However, especially carbon ions ($Z=6$) have become of peculiar interest in recent times due to their LET-properties. They warrant a high-LET quality within the Bragg peak because of the higher ionization densities, which corresponds with a higher RBE, and a low-LET behaviour at the entrance of the biological tissue to spare normal tissue.

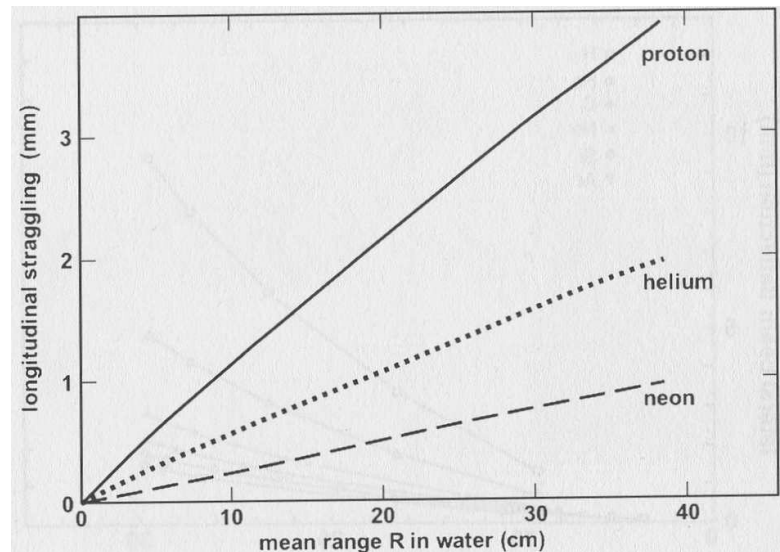


FIGURE 1.10: Straggling effect of various ions ([24],p.49)

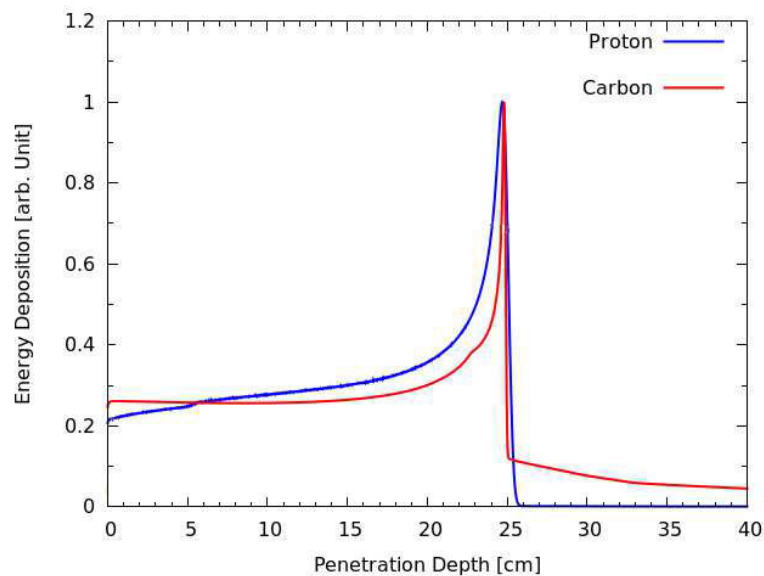


FIGURE 1.11: Dose deposition as a function of the penetration depth of protons and carbon ions

1.2 Volume concepts

It is the main rationale of radiotherapy to deliver the prescribed dose to the tumor volume that conforms the tumor as closely as possible while reducing the dose to the surrounding normal tissue. Especially, the dose to the organs at risks (OAR) in the vicinity of the tumor, should be as low as possible to reduce side effects and complications of normal tissue. This endeavour is known as "ALARA"-principle. "ALARA" is an acronym for

"As Low As Reasonably Achievable" and represents a regulatory requirement for all radiation safety programs and defined as following:

"For all medical exposure of individuals for radiotherapeutic purposes, exposures of target volumes shall be individually planned; taking into account that doses of non-target volumes and tissues shall be as low as reasonably achievable and consistent with the intended radiotherapeutic purpose of the exposure." (Directive 97/43/EURATOM, Article 4)

To fulfil these requirements, imaging devices with a suitable resolution are necessary to identify the tumor volume and the organs at risk. Moreover, accelerators for accurate beam delivery and software tools for dose calculations are required.

Since the 1960s, the first computers which were capable of calculating dose distributions were available. In the 1970s, the modern imaging methods by means of computer tomography (CT) and magnetic resonance imaging (MRI) were established and subsequently introduced into Radiotherapy.

1.2.1 Volume concepts in radiation oncology

The localization and the extent of the tumor volume are determined by imaging modalities like CT and MRI. Thus, 3-D anatomical informations in terms of closely spaced transverse images serve as basis for structure delineation. The visible tumor and the organs at risk are outlined slice by slice by radiation oncologists.

For the treatment planning process itself a CT-image data-set is required, since the densities of the tissue are required for the dose calculation taking into account tissue heterogeneities.

The following delineated volumes are based on the recommendation by the ICRU Report No.50 [38](Figure 1.12).

Gross Tumor Volume (GTV)

"The Gross Tumor Volume (GTV) is the gross palpable or visible/demonstrable extent and location of malignant growth." (ICRU Report No.50)

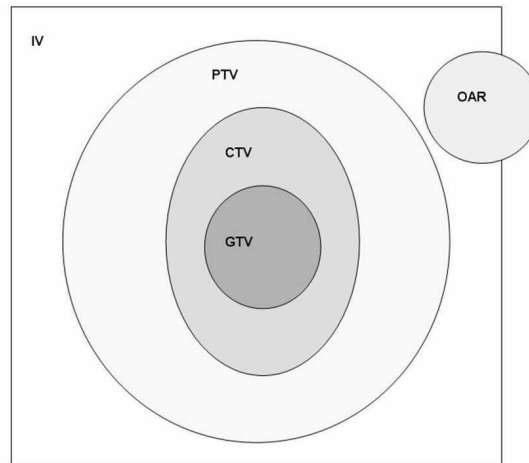


FIGURE 1.12: Various treatment volumes

Clinical Target Volume (CTV)

"The Clinical Target Volume (CTV) is a tissue volume that contains a GTV and/or subclinical microscopic malignant disease, which has to be eliminated. This volume thus has to be treated adequately in order to achieve the aim of therapy: cure or palliation." (ICRU Report No.50)

Planning Target Volume (PTV)

"The Planning Target Volume (PTV) is a geometrical concept, and it is defined to select appropriate beam sizes and beam arrangements, taking into consideration the effect of all the possible geometrical variations and inaccuracies in order to ensure that the prescribed dose is actually absorbed in CTV." (ICRU Report No.50)

Irradiated Volume

"The Irradiated Volume is that tissue volume which receives a dose that is considered significant in relation to normal tissue tolerance." (ICRU Report No.50)

Organs at risk (OAR)

"Organs at risk are normal tissues whose radiation sensitivity may significantly influence treatment planning and/or prescribed dose." (ICRU Report No.50)

These anatomical structures are an integral component of every optimization process in treatment planning. The aim is to spare the OAR from to high dose exposure. Due to that, the search of an adequate dose coverage of the PTV and a satisfying OAR dose sparing is a complex balancing act.

More detailed informations about volume concepts in radiation oncology can be found in “The Physics of Radiation Therapy” ([34],chapter 11.8).

1.2.2 Dose-volume histogram (DVH)

A DVH represents a concept in radiation treatment planning which illustrates a 3-D dose distributions of a target volume, an organ at risk or an arbitrary structure in a graphical 2-D format. The generation of a DVH is done by the determination of the dose bin size of the histogram. The bin doses are depicted along the horizontal axis, the structure volumes on the vertical.

DVHs can be divided into differential DVHs and cumulative DVHs. The differential DVH illustrates the dose which was received by the volume concerning each bin. The higher the column of a bin, the more dose was received. The cumulative DVH is a mapping that counts for a volume the cumulative number of the received doses in all of the bins up to the specified bin. Thus, the column height of each bin on the horizontal axis represents the volume receiving greater than (or equal) to that dose. Figure 1.13 illustrates a cumulative DVH for planing target volumes.

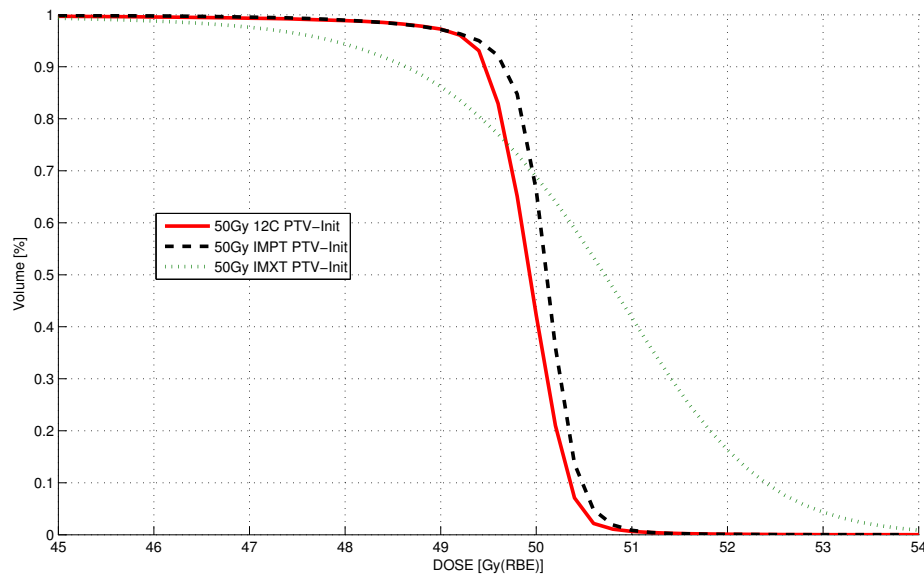


FIGURE 1.13: Cumulative DVH of a planning target volume

For the illustration of the results of the present study only cumulative DVHs were used.

1.3 Delivering systems in radiation therapy

The next chapters provide an overview about accelerators, whereas the chapter describes both accelerators for photon and for light ion beam radiotherapy. More information can be found in "The Physics of Radiation Therapy" ([34],chapter 4.3), in "The Handbook of Radiotherapy Physics" ([14],chapter 11.1-11.3) in "Kernphysik" ([22],chapters 5.4.3-5.4.4) and in "Experimentalphysik 4" ([23],chapter 4.1.5).

1.3.1 Linear accelerator (LINAC)

A linear accelerator is a device which is used to accelerate electrons in a linear tube by means of high frequency electromagnetic waves. It consists of an energy supply, which provides direct current DC to the modulator which contains a pulse-forming network and a switch tube. The modulator transfers high voltage pulses to both, the magnetron and the electron gun (Figure 1.14). The magnetron is a high power oscillator, which generates microwave pulses and applies them to the acceleration tube via waveguide system. The electron gun consists either of a cold cathode, a hot cathode or a photo cathode. After the injection into acceleration tube the electrons gain energy from the sinusoidal electromagnetic field of the microwaves and undergo the accelerating process.

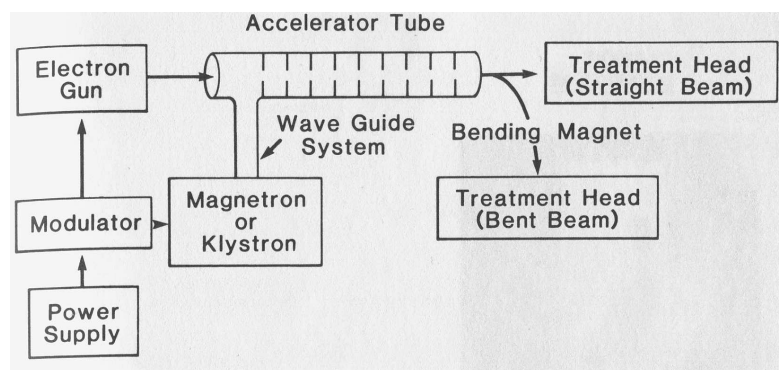


FIGURE 1.14: Setup of a LINAC ([34],p.43)

After the acceleration of the electrons, they are led by means of bending magnets into the treatment head, where they are shot onto an absorbing, water cooled target with high Z like tungsten. As a consequence of the interaction of electrons and the target, bremsstrahlung is produced. The bremsstrahlung is characterized by an X-ray spectrum corresponding to the maximum energy of the incident electrons. The treatment head

consists of a primary filter, primary collimator, flattening filter, ion chambers, multi-leaf collimator and jaws, which prepare the photon beam for the radiotherapy.

1.3.2 Pre-accelerators for light ions

The linear accelerators with the purpose of pre-acceleration of light ions before the injection to circular accelerator like synchrotron are constructed differently. The acceleration tube (a hollow pipe vacuum chamber) consists of several consecutively arranged, hollow cylindrical electrodes, also known as drift tubes. These drift tubes changes their charge very quickly because of a high frequency alternating current (AC). As a consequence of that, the particles are accelerated in the gaps between the electrodes. While they traverse an electrode, where there is no field due to a shielding, the pole of the electrodes changes. Furthermore, the length of the electrodes is conformed to the velocities of the accelerated particles to warrant losses (Figure 1.15). After reaching the desired velocity, the ions are injected into a higher energy accelerator like a synchrotron.

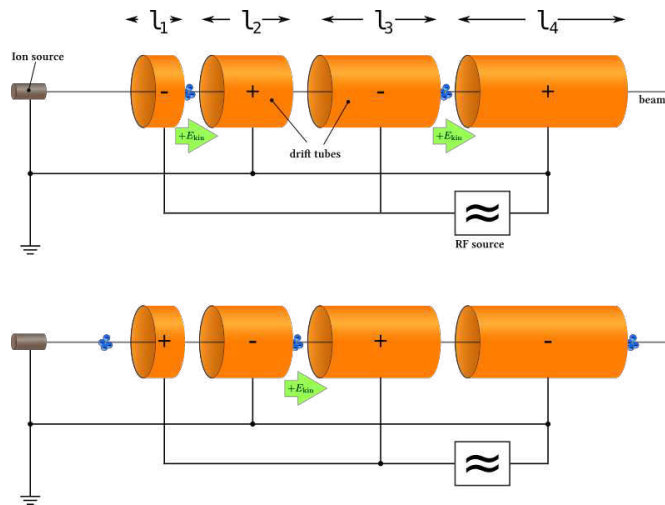


FIGURE 1.15: Drift tube arrangement of a LINAC [22],p.163

1.3.3 Cyclotron

A cyclotron is a circular accelerator with a changing field. It consists of one magnetic dipole field. Between the poles of this field two evacuated half cylindrical electrodes (dees) are arranged, which form the poles of the electric field. In the gap between the two dees a high frequency voltage U is applied. By means of an ion source in the center of the magnetic field, the ions are generated and accelerated in the electric field in the gap between the dees. Due to the non existing field within the dees, the ions undergo

a semicircular movement with the radius r as a consequence of the equilibrium between the Lorentz-force resulting from the magnetic field B and the centripetal force:

$$\frac{m * v^2}{r} = q * v * B \quad (1.16)$$

m represents the mass of the ion, v the velocity and q the charge.

Through including the angular velocity ω the condition of the cyclotron can be formulated:

$$\omega = \frac{q * B}{m} \quad (1.17)$$

Thus, it can be shown that the time t for the semicircular movement is independent from the radius:

$$t = \frac{\pi * r}{v} = \frac{\pi * m}{q * B} \quad (1.18)$$

Due to that constant high frequency f_{HF} can be used:

$$2\pi * f_{HF} = \omega_{HF} = \frac{q * B}{m} \quad (1.19)$$

Resulting from 1.18 the ions reaching the accelerating gap between the dees after a constant period of time and gain after passing the gap a constant quantity $q * U$ of energy. The radius increases simultaneously with the velocity according to 1.16. As a consequence of that, the ions undergo a spiral movement consisting of semicircles with increasing radius up to the edge of the cyclotron at a radius R , where a electrical bending field extracts the ions out of the cyclotron.

Thus, the maximum of the kinetic energy E_{kin} is:

$$E_{kin} = \frac{m * v^2}{2} = \frac{q^2}{2 * m} (R * B)^2 \quad (1.20)$$

The limit of energy is at about 30 MeV for protons. Higher energies cause the effect of relativistic mass increase. Due to that, the condition 1.18 can't be fulfilled any more.

To overcome this limit, however, synchro-cyclotrons were developed in order to modulate the acceleration frequency with the radius and the relativistic particle mass increase.

1.3.4 Synchrotron

Before the tangential injection of the ions into the synchrotron, they are pre-accelerated in a LINAC up to velocities of 0.8-0.99 c. After the injection the particles follow a circular orbit of constant radius inside a vacuum chamber.

The orbit is determined by cyclic arranged field magnets. Practically, dipole deflecting magnets are alternating with linear parts of the track to facilitate arrangements of accelerating fields and magnetic focusing and defocusing fields resulting from the quadrupole. Sextupole are responsible for the beam transport corrections. Both the high frequency and the magnetic field strength of the dipoles have to vary over time, to warrant the same cyclic tracks for particles with relativistic mass increase. Furthermore, they have to be injected in the form of a bunch to exceed a minimum of energy for the further acceleration. On their circular path, the particles are passing through areas of strong and weak magnetic fields, which leads to a beam focusing. In Figure 1.16 the arrangement of injection part, accelerating areas, bending magnets and focussing magnets is shown.

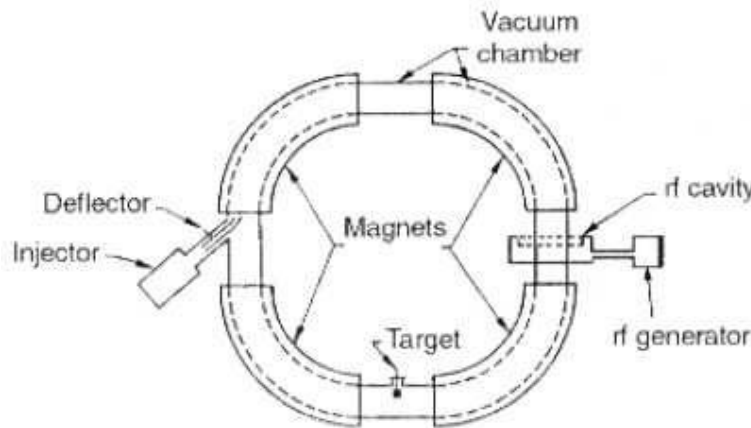


FIGURE 1.16: Set-up of a synchrotron

By means of a synchrotron energies up to a range of TeV (10^{12} eV) can be achieved.

In Figure 1.17 an acceleration system with a pre-accelerating LINAC and a synchrotron for medical applications is illustrated for the Heidelberg Ionenstrahl-Therapiezentrum (HIT).

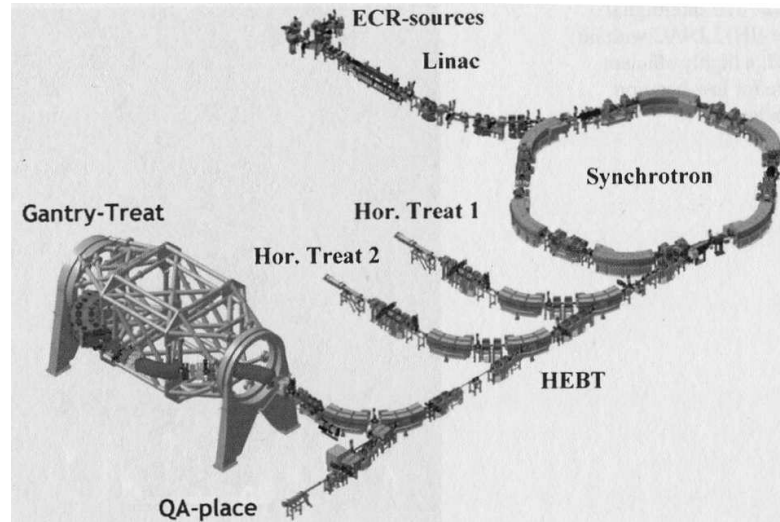


FIGURE 1.17: Arrangement of a synchrotron in conjunction with LINAC and treatment areas ([24],p.335)

1.4 Passive scattering and active scanning

The major rationale of radiation therapy is to achieve a satisfying coverage over the entire target volume. In order to obtain this for light ion therapy, two different techniques exist for clinical implementation to spread out the Bragg peak: passive scattering and active scanning.

1.4.1 Passive scattering

Passive scattering uses external scattering material in order to spread out narrow beams up to the magnitude of the desired target volume [39]. The beam broadening can be realized by scattering foils. Moreover, the field aperture is regulated by collimators and the distal edge of the high dose volume is determined by individual compensators.

A homogeneous depth dose distribution is obtained by a ridge filter or a spinning wheel of variable thickness, which causes superposition of beams with slightly different energies.

In Figure 1.18 the passive scattering is illustrated for a proton pencil beam and its characteristic dose distribution, called Bragg peak. The superposition of Bragg peaks with slightly different energies is called spread out Bragg peak.

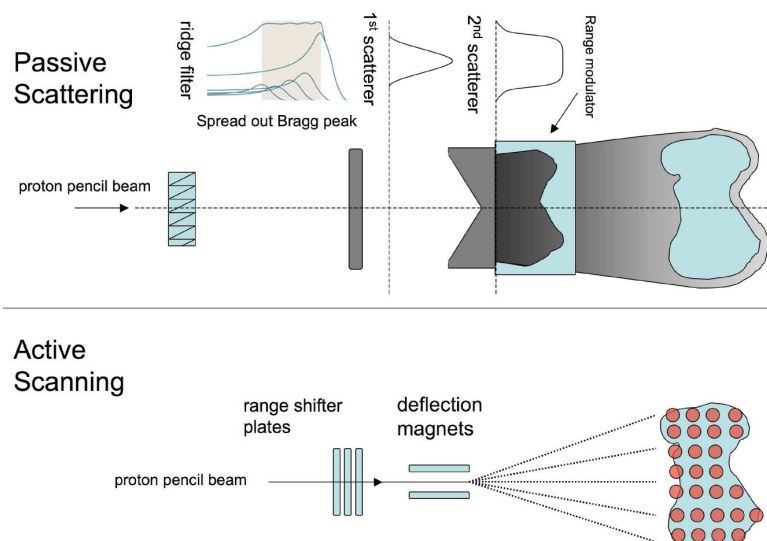


FIGURE 1.18: Principle of passive scattering and active scanning proton beam delivery [39]

1.4.2 Active scanning

In the active scanning technique, the pencil beam is actively scanned over the desired tissue for the treatment by deflection with bending magnets 1.18.

Thereby, a dose deposition in small spots over the target volume takes place, which leads to a range modulation for individual spots by the variation of the incoming pencil beam energies. Thus, different initial particle energies are required.

Compared to the passive scattering technique, the depth of dose deposition is much more sensitive and the scattered radiation is reduced. Furthermore, the active scanning method enables the application of intensity-modulated treatment techniques [40].

1.5 Dose calculation algorithms

After the delineation of the target and the anatomical structures, treatment fields as well as beam arrangements are designed and the dose distribution is optimized according to the clinical objectives using a commercial treatment planning system (TPS). In order to optimize a treatment plan appropriately, beam directions, field numbers, beam weights, intensity modifiers and an optimal field aperture is required. Different treatment planning algorithms are available for the realization of these issues.

In this chapter four treatment planning algorithm are described in detail: correction-based, model-based, pencil beam and direct Monte Carlo. All of them can be used for

3-D treatment planning with varying accuracy and speed. However, the model-based and the Monte Carlo-algorithm are the most promising one due to the simulation of the radiation transport and the prediction of the dose distribution under the conditions of charged particle equilibrium in tissue with low density.

This chapter is based on the “Handbook of Radiotherapy Physics” ([14],chapter 23), “The Physics of Radiation Therapy” ([34],chapter 19-20) and ”Ion beam therapy” ([24], chapter 30.5.1).

1.5.1 Correction-based algorithms

These algorithms are based on measured data and represents semi-empirical algorithms. Diverse correction factors and functions are applied in order to calculate the dose distribution in the patient.

The corrections are in terms of the attenuation, scattering and geometry. The attenuation corrections are due to contour irregularities or beam intensity modifiers. The scattering corrections depend on the scattering volume, the field size, the form and the radial distance.

These algorithms includes on the one hand methods which interpolate measured depth-dose data and on the other hand methods with specially formulated functions which predict the correction factors under specified conditions.

The limitation of these algorithms is concerning 3-D heterogeneity corrections in tissue interfaces and tissues with low densities.

1.5.2 Model-based algorithms

This algorithms are based on the calculation of the dose distribution by means of a physical model, which simulates the radiation transport. Model-based algorithms are capable to model primary photon energy fluence incident at a point and the energy distribution as a consequence of primary photon interactions. Furthermore, they can simulate the transport of scattered photons and electrons away from the interaction site.

One type of model-based algorithm is the so called convolution-superposition method. This method uses convolution equations which consider both the transport of primary photons and the transport of scattered photons and electrons resulting from interactions of the former one. The dose calculated $D(\vec{r})$ is illustrated in formula 1.21.

$$D(\vec{r}) = \int \frac{\mu}{\rho} \Psi_P(\vec{r}') A(\vec{r} - \vec{r}') d^3 \vec{r}' = \int T_P(\vec{r}') A(\vec{r} - \vec{r}') d^3 \vec{r}' \quad (1.21)$$

\vec{r} represents the position of the point, μ/ρ the mass attenuation coefficient, $\Psi_P(\vec{r}')$ the primary photon energy fluence and $A(\vec{r} - \vec{r}')$ the convolution kernel. The convolution kernel corresponds to a matrix of dose distribution by scatter photons and electrons resulting from interactions of primary photons. The product of μ/ρ and $\Psi_P(\vec{r}')$ is $T_P(\vec{r}')$, also called Terma, and corresponds to the total energy released per unit mass. Terma is related to Kerma 1.3. The integrated product over a volume of Terma and the convolution kernel gives the dose $D(\vec{r})$ as shown in 1.21.

Formula 1.21 modified for radiological path length gives the convolution-superposition equation:

$$D(\vec{r}) = \int T_P(\rho_{\vec{r}'} * \vec{r}') A(\rho_{\vec{r}-\vec{r}'} * (\vec{r} - \vec{r}')) d^3 \vec{r}' \quad (1.22)$$

$\rho_{\vec{r}'} * \vec{r}'$ represents the radiologic path length from the source to the primary photon interaction site and $\rho_{\vec{r}-\vec{r}'} * (\vec{r} - \vec{r}')$ the radiologic path length from the site of primary photon interaction to the site of dose distribution.

1.5.3 Pencil beam algorithm

The pencil beam algorithm divides the main beam for the treatment into sub-beams, the so called pencil beams.

The dose calculation for the pencil beam algorithm is separated into two parts:

- the depth dose calculation along the central axis of the beam
- the lateral or "off-axis" distribution

In other words:

"The pencil beam [...] $[P_{(x,y,z,E_0)}]$ is defined as the dose deposited in a semi-infinite water phantom by an infinitely narrow beam of incident particles with initial energy E_0 at depth z and radial distance [...] $[x,y]$ from the central

axis. In particular, this distribution includes the dose due to particles that are scattered away from the central axis.” ([24],p.513)

Up to tens of thousands of narrow particle beams (spots) are used for irradiation in active scanning. Every pencil beam is weighted and is so directly proportional to the particle fluence of the beam for the pencil's position.

The total dose results from superposition of all pencil beams. This can be done by the integration over the beam aperture and energy spectrum. In the case of scanning pencil beams, the primary beams can be seen as discrete pencil beams and the dose calculation reduces itself to a weighted sum. All pencil beams (PB_i) at a given point within the range of three times the spot sigma are taken into account [41].

$$D(x, y, z) = \sum_{PB_i \in [-3\sigma; +3\sigma]} D_{CAX,i}(x_0, y_0, z_0) * F_i(x - x_0, y - y_0, z - z_0) \quad (1.23)$$

$D_{CAX,i}$ represents the dose to be delivered by a pencil beam at the central axis (CAX) at (x_0, y_0, z_0) and F_i the relative fluence distribution of the considered pencil beam at the calculation point of the dose (x, y, z) .

The main differences between the pencil beam algorithms for photons and ions are the kind of interactions.

For the ions, for example, the depth dose calculation along the central axis is determined by the energy losses due to ionization, whereas the lateral or "off-axis" distribution is determined by multiple Coulomb scattering of the incident particles, represented by σ . However, the pencil beam algorithm can handle both multiple Coulomb scattering and the energy losses of the individual beams, but needs an empirical handling concerning more complex effects as nuclear fragmentation or lateral inhomogeneities.

The off-axis distribution for particle beams can be considered as a Gaussian distribution:

$$F(x, y, z, E_0) = \frac{1}{2\pi\sigma_{(x,y,E_0)}^2} \exp\left(-\frac{(x - x_0)^2}{2\sigma_{(x,y,E_0)}^2} - \frac{(y - y_0)^2}{2\sigma_{(x,y,E_0)}^2}\right) \quad (1.24)$$

The reason why F is depending on z is due to energy and depth dependent corrections for the spot $\sigma_{(z,\sigma_0)}$, whereas σ_0 represents the initial spot in air.

Concerning photons, the Pencil beam algorithm divides an intensity-modulated field into finite-size elements and integrates the dose of all finite-size pencil beams. Additionally, the formalism also takes the relative weight of each pencil beam into account. The main limitations are heterogeneities and scatter dose calculations for phantom sizes deviating substantially from sizes for which the pencil beam has been determined.

1.5.4 Monte Carlo algorithm

The Monte Carlo technique is a computational method, which is capable of simulating the transport of millions of photons and particles through matter employing statistical methods. In radiation therapy it is used for the calculation of the dose distribution in biological tissue. The methodology of this algorithm is to determine the propagation of the radiation by means of the theory of probability. The propagation depends on the types of radiation and their energies as well as the density and the chemical composition of the irradiated tissue.

Due to the fact that the interaction of radiation with matter is a stochastic process, the Monte Carlo algorithm is predestined to simulate the probable direction and energy distributions of every single particle of the radiation. The higher the number of simulated particles is, the higher is the statistical accuracy.

Mathematically, for the description of the trajectories of particles the linear Boltzmann transport equation is used [42]:

$$\left[\frac{\partial}{\partial s} + \frac{p}{|p|} \frac{\partial}{\partial x} + \mu(x, p, s) \right] \psi(x, p, s) = \int dp' \mu(x, p, p') \psi(x', p', s) \quad (1.25)$$

x is the position and p is the momentum of the particle. $(p/|p|)d/dx$ represents the directional derivative, s the path length, $\mu(x, p, p')$ the macroscopic differential cross section and $\psi(x', p', s)$ the probability of presents.

To solve this transport equation the Monte Carlo algorithm needs to be applied. In the Monte Carlo algorithm an integral for a random function f in the volume V can be estimated through N randomly chosen points x_1, x_2, \dots, x_N by means of:

$$\int f dV \approx V_{\langle f \rangle} \pm V \sqrt{\frac{\langle f^2 \rangle - \langle f \rangle^2}{N}} \quad (1.26)$$

With

$$\langle f \rangle = \frac{1}{N} \sum_{i=1}^N f(x_i) \quad (1.27)$$

And

$$\langle f^2 \rangle = \frac{1}{N} \sum_{i=1}^N f^2(x_i) \quad (1.28)$$

This is the central theorem of the Monte Carlo integration [43]. If the parameters for radiation-matter interactions are determined (for the Compton effect, for example, the Klein-Nishina formula is used), the transport equation in a medium can be solved by Monte Carlo algorithm. According to 1.26 the accuracy of the calculation is proportional to the amount of the randomly chosen points.

1.6 Treatment techniques

Basically, two different approaches of treatment planning processes can be divided: forward and inverse planning.

For the generation of treatment plans, the forward planning technique can be used in external beam radiotherapy. To perform forward planning, the number of beams, the prescribed dose for each beam, the beam directions and the MLC configurations to shape the beam according to the tumor shape from the beam's eye view have to be set. The weighting of the beam directions has to be done manually in order to fulfil the dose prescription to the target.

In the inverse planning process, the fluence profiles are optimised from each beam direction by a minimization of an objective function [44, 45]. After the optimization, each profile is transformed into a series of segments, which are determined by the treatment planning system to realize optimized fluence maps. The segments or leaf movement patterns for dynamic delivery can be delivered with a multi-leaf collimator (MLC). Thus, the segment shapes are not defined manually and the number of segments is always larger, when compared to forward planning.

In Figure 1.19 the difference between forward planning and inverse planning is illustrated.

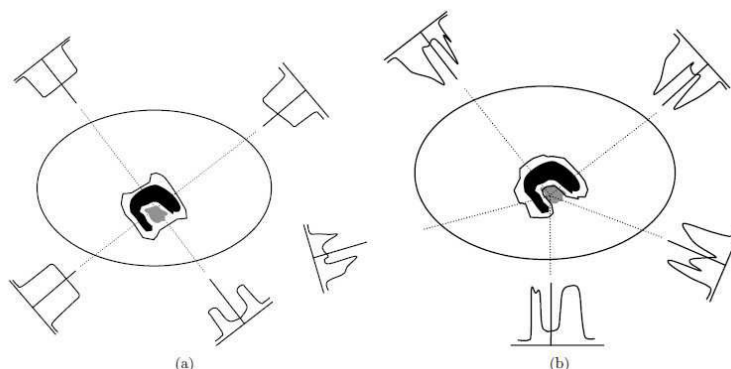


FIGURE 1.19: Comparison of forward planning and inverse planning [46]

In this chapter, several treatment techniques are described. The basis for conformal radiotherapy (CRT) and the single-field uniform dose (SFUD) is forward planning, whereas intensity modulated X-ray therapy (IMXT) and intensity modulated proton therapy (IMPT) use the inverse planning approach.

All these treatment techniques are explained in more detail in the “Handbook of Radiotherapy Physics” ([14],chapter 43-45), “The Physics of Radiation Therapy” ([34],chapter 20.1-20.3) and ”Ion beam therapy” ([24],chapter 30.6).

1.6.1 Conformal radiotherapy (CRT)

The conformal radiotherapy (CRT) delivers a constant photon fluence and uniform doses across the treatment field of one beam. The geometrical shape of the field is defined by the multi-leaf collimator.

Resulting from the rationale of radiotherapy to achieve a good dose-coverage of the target volume, CRT aims for the delivery of a defined dose to fulfil the dose prescriptions to the target volume.

Beam directions and beam weights are defined manually by means of trial and error processes based on human intelligence. The CRT treatment planning method is based on the principle of forward planning. Thus, the configuration of the beam directions and beam weights represents the only way of optimizing the dose exposure of normal tissue.

Conformal radiotherapy treatment plans are limited by the distribution of fluence within the collimator boundaries of the incident beams.

1.6.2 Intensity modulated X-ray therapy (IMXT)

In the intensity modulated X-ray therapy (IMXT), a non-uniform energy fluence ψ is applied to the patient from any given position to generate the desired dose distribution. The fluence is defined as it is shown in the formula 1.29.

$$\psi = \frac{dR}{dA} \quad (1.29)$$

dR represents the radiant energy incident on a sphere of cross-sectional area dA .

The advantage of non-uniform beam intensities is the better conformation around the target volume because of the varied intensity (fluence) of the primary beams. An optimal fluence profile for a set of beam directions is realized by inverse planning, which enables dose sculpting with aid of intensity modulation.

The requirements for clinical applications of IMXT are twofold: On the one hand a treatment planning system for the calculation of the non-uniform fluence maps, and on the other hand a delivery system for these planned fluence maps are required. However, the process of treatment planning demands an optimization of the constraints. Planning constraints are the prescribed dose to the target and dose limits for the organs at risk.

In order to produce intensity modulated fluence profiles, the linear accelerator has to be equipped with a system, which is capable of transforming a beam profile into a profile of arbitrary shape. The MLCs define and subdivide the beam into beamlets with uniform beam intensities, which are the basis for the variation in fluence. These subfields are created by the MLCs.

Conventional MLCs can be divided into segmental or dynamic MLCs. The segmental MLC represents static leaves, while the dynamic MLC is capable of moving its leaves during the radiation delivery process. Consequently, the dynamic MLC enables a close matching of the delivered intensity with the optimal fluence. Thus, accurate preservation of both the spatial and intensity resolutions is obtained [47].

The optimum number of segments and the weighting of the beamlets are calculated by the treatment planning system.

1.6.3 Single-field uniform dose (SFUD)

The single-field uniform dose (SFUD) is a treatment planning method for protons or light ions. It optimizes single treatment fields separately to deliver a homogeneous and uniform dose across the target volume. Each beam is weighted manually and summed up.

SFUD can be performed with both passive scattering and active scanning and represents an easy and robust method for treatment plan calculation in a minimum of time. Moreover, with SFUD only a weak constraints-inclusion for organs at risk is possible.

1.6.4 Intensity modulated proton therapy (IMPT)

IMPT is based on the same principle like IMXT with spots instead of segments. It is a method which optimizes simultaneously all treatment fields in a plan including all scanned spots and it is performed in combination with active beam scanning. However, the modulation is more focussed on the number of particles and not on the beam intensity itself.

The IMPT calculation process can be characterized by the simultaneous optimization of all Bragg peaks.

Moreover, IMPT plans can be optimized using dose-volume constraints in order to enable a selective sparing of specific organs at risk [48]. Consequently, the individual fields can reveal an inhomogeneous dose distribution with high in-field dose gradients. Without any dose constraints, the IMPT plan consists of single fields with a quasi-homogeneous dose distribution [49].

Compared to SFUD the IMPT method needs more time for the computing process and more memory as a consequence of the particle numbers at 30.000-50.000 scan spots per field which are included in the optimization in terms of the isoeffective dose. Due to that, a sampling of a large fragmentation database for each scan spot is involved. Thus, IMPT enables an enhanced proof to geometrical errors.

Chapter 2

Patients and methods

In this chapter the methodology used in this study is introduced. Additionally, fundamental medical as well as technical aspects are described. Particularly, a description of the used planning treatment systems and the evaluation software is given.

2.1 Medical aspects

2.1.1 Meningioma

Meningioma is the second most widespread type of brain cancer and represents 15-25% of all intracranial neoplasm [50]. About 5-10% of the meningioma consist of non-benign histology and are therefore atypical or anaplastic meningiomas. These meningiomas reveal an aggressive local growth and an early recurrence or a high tumor progression after surgery [51]. As a consequence, neurosurgical resections on their own do not provide a long-term tumor control and do not correspond with a high survival rate [52].

Basically, the resection level is classified according to the Simpson-grading as shown in Table 2.4.

Radical	
Stage 1	complete excision, including dura and bone
Stage 2	complete excision + supposed reliable coagulation of dural attachment
Non-Radical	
Stage 3	complete excision but insufficient dural coagulation or bone excision
Stage 4	incomplete excision, macroscopic rest visible (on MRI)
Stage 5	biopsy only (visible on MRI)

TABLE 2.1: Simpson grading for Meningioma[53]

Non-radical resections reveal a worse outcome when compared to radical resections [54]. The local recurrence rates in patients with non-benign meningiomas are 50% for those who were subtotally excised and 90% for those who were completely resected at 3 years. Furthermore, a high recurrence rate correlates with a higher lethal rate.

However, adjuvant radiation therapy has proven effective when combined with surgery [55, 56]. Former studies delivered promising outcomes after postoperative radiotherapy as opposed to surgery alone for patients with non-benign meningiomas [53]. With intensity-modulated radiotherapy, for example, high local tumor control rates with up to 95% were reached [57, 58].

2.2 Patients

This study included 10 patients (MA) with skull base meningioma with an age ranged from 37 up to 81 years at the time of the initial diagnosis. Nine of the patients were female (90%) and one male (10%). The localization of the tumors was at the sphenoid bone for three patients, for each two patients at the fossa cranii media and the sinus cavernosus and for each one at the dorsum sellae, the fossa pterygopalatina and the spehenoorbita.

All patients were treated with conformal photon radiotherapy at the Medical University of Vienna/AKH Wien before this study started.

2.2.1 Target volumes

The GTV consists of the primary tumor and metastases and thus has a high density of tumor cells (more than $10^6 mm^{-3}$). The GTV as the macroscopically visible tumor extent (see chapter 1.2.1) is determined on both computer tomography and contrast enhanced magnetic resonance imaging [59].

Table 2.1 and Figure 2.1 illustrate the definition of the $CTV_{initial}$, $PTV_{initial}$ and PTV_{boost} based on the GTV used in this study.

	Definition
$CTV_{initial}$	GTV + margin of 1cm adapted to the surrounding tissue
$PTV_{initial}$	$CTV_{initial}$ + isotropic margin of 3 mm
PTV_{boost}	GTV + isotropic margin of 3 mm

TABLE 2.2: Definition of the target volumes

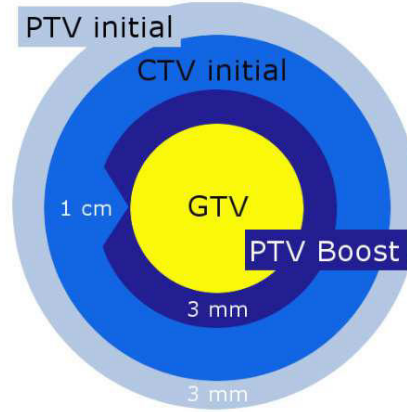


FIGURE 2.1: Graphical depiction of the target volumes

The median macroscopic size (GTV) of the tumor was 49 cm^3 , ranging from 11 up to 111 cm^3 .

The median $\text{PTV}_{\text{initial}}$ was $147 \pm 85 \text{ cm}^3$ (range of 44 up to 272 cm^3) and the median $\text{PTV}_{\text{boost}}$ was $94 \pm 46 \text{ cm}^3$ (range of 31– 182 cm^3). Examples of delineated target volumes can be seen in figure 2.2.

	MA1	MA2	MA4	MA6	MA7	MA8	MA9	MA10	MA11	MA12
PTV_{init}	55.0	77.4	272.4	175.1	179.2	119.6	260.7	198.3	44.3	107.6
PTV_{boost}	26.4	49.1	182.0	111.7	111.9	75.9	181.2	120.2	30.8	45.2
GTV	11.5	23.0	97.6	62.2	61.2	36.9	111.1	66.8	14.5	20.5

TABLE 2.3: Absolute tumor volumes in cm^3 of PTVs and GTV of all meningioma patients

The values of the tumor extent of each patient are shown in table 2.2, whereas the mean and median volumes over all patients are shown in table 2.3.

	Mean	Median	1. Quartile
PTV_{initial}	149	147	85
PTV_{boost}	93	94	46
GTV	51	49	21

TABLE 2.4: Statistical tumor volumes in cm^3 of PTVs and GTV

2.2.2 Organs at risk (OAR)

Organs at risk can be divided due to their anatomical incidences. Delineated OAR which occur at each brain hemisphere can be indicated with the terms ipsilateral (i) and contralateral (c) (Table 2.6). In this study beside the primary organs at risk also

so called secondary organs were delineated for an adequate sparing of normal tissue as described in chapter 1.2.1.

Primary OAR		Secondary OAR	
Chiasm		Hippocampus	i and c
Eye	i and c	Hypothalamus	i and c
Optical Nerve	i and c	Cochlea	i and c
Cerebellum		Brain hemisphere	i and c
Brainstem		Lense	i and c
Temporal Lobe	i and c		
Hypophysis			

TABLE 2.5: List of OAR included in this study

Two examples of OAR delineation on post-surgery magnetic resonance images are shown in Figure 2.2. Beside various OAR also the delineated PTV (red) and the GTV (violet) can be seen.

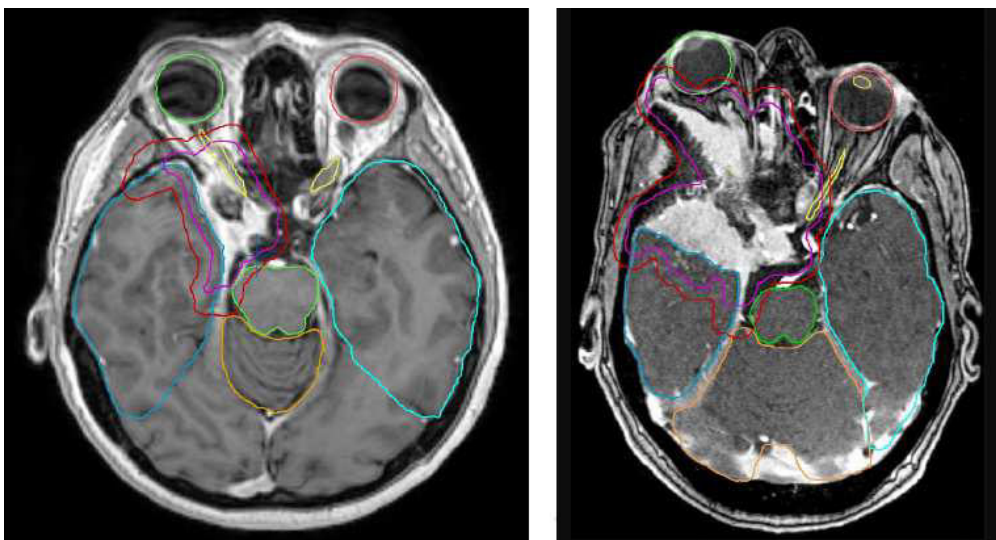


FIGURE 2.2: Delineation of PTV, GTV and OAR

Basically, dose limits were available for various OAR, which were taken into account in this treatment planning study. Unfortunately, not all of those dose limits were suitable to be used in this study, since in most former studies a lower dose for the PTV was prescribed, which ranged from 50 Gy(RBE) to 54 Gy(RBE). The prescribed dose of the summed up plans in this study was 68 Gy(RBE) because of considerations by former studies which suggested a prescribed dose higher than 60 Gy(RBE) in order to cause the death of the malignant tumor cells [53]. Thus, the dose limits were not directly applicable if a certain OAR was localized within or in the vicinity of the PTV.

Some constraints are shown in the following list:

- chiasm $D_{mean} < 54 \text{ Gy(RBE)}$
- chiasm $D_2 < 60 \text{ Gy(RBE)}$
- optical nerves $D_{2\%} < 60 \text{ Gy(RBE)}$
- brainstem $D_{mean} < 53 \text{ Gy(RBE)}$
- eye $D_{mean} < 6.1 \text{ Gy(RBE)}$
- eye $V_{35} < 50 \text{ Gy(RBE)}$
- lens $D_{2\%} < 6 \text{ Gy(RBE)}$
- cochlea $D_{mean} < 45.1 \text{ Gy(RBE)}$
- hypophysis $D_{2\%} < 50 \text{ Gy(RBE)}$

The detailed definition of each parameter is given in chapter 2.6.2.

2.3 Treatment planning systems

The three treatment techniques which were introduced in chapter 1 were used in this study: intensity-modulated X-ray therapy (IMXT), intensity-modulated proton therapy (IMPT) and carbon ion therapy (^{12}C). The prescribed dose was 50 Gy(RBE) in 25 fractions and 18 Gy(RBE) in 6 fractions for $PTV_{initial}$ and PTV_{boost} , respectively.

The following combinations of $PTV_{initial}$ and PTV_{boost} were considered to deliver the total summed up dose of 68 Gy(RBE):

Initial plans	Boost plans		
IMXT	IMXT	IMPT	^{12}C
IMPT	IMPT	^{12}C	
^{12}C	^{12}C		

TABLE 2.6: Combination of various treatment techniques for this study

The utilized treatment planning systems were Monaco V.3.2 (Elekta CMS software, St. Louis, MO) for the IMXT plans, XiO V.4.4.1 (Elekta, CMS software, Crawley, UK) for the IMPT plans and TRiP98 V.1001c for the ^{12}C plans.

The degrees of freedom were defined by the couch angle and the gantry angle for each beam. For IMPT and ^{12}C no rotating gantry was assumed. Thus, the light ion scenarios were based on fixed beam lines with a constant gantry angle.

The main challenge of creating treatment plans was to find the optimal beam angles to obtain an adequate dose coverage of at least 95% of the $PTV_{initial}$ and the PTV_{boost} with 95% of the prescribed dose and a low dose exposure of the primary OAR. The maximum allowed dose to both target volumes were 107% of the prescribed dose corresponding to 53.5 Gy(RBE) for the initial treatment plans and 19.3 Gy(RBE) for the boost plans, respectively [46].

2.3.1 Monaco

In this study the treatment planning system Monaco V.3.2 (Elekta CMS software, St. Louis, MO) was used to create IMXT plans. The optimization process of the treatment plans was done by means of biological or physical cost functions and physical dose-volume constraints in order to optimize the dose distribution in the target volume (PTV) and anatomical structures (OARs). For each structure one or more cost functions can be assigned.

The first part of the optimization process represents the calculation of the optimal fluence distribution for all beams by solving the optimization problem. This is done with the conjugate gradient algorithm. Additionally, the corresponding dose distribution of a finite pencil beam algorithm is calculated.

The second part of the optimization process is the beam segmentation according to the weight of the beam and the mechanical MLC-properties [60].

Furthermore, a recalculation of the dose distribution with the use of a Monte Carlo simulation is performed [61]. The optimization process concerning the shaping of the segments lasts until a satisfying dose distribution according to the cost functions and their constraints is obtained [60].

2.3.1.1 Cost functions

The cost functions can be divided into 5 physical and 3 biological cost functions.

Physical cost functions:

- Quadratic overdose: Prevention for hot-spots
- Quadratic underdose: Prevention for cold-spots
- Maximum dose: Fixing of a dose limit which must not be exceeded

- Overdose DVH: only a certain percentage of volume is allowed to exceed a certain dose
- Underdose DVH: only a certain percentage of volume is allowed to be below certain dose
- Target penalty: implements a quadratic penalty which starts at a certain dose threshold.

Biological cost functions:

- Target-EUD: Prevention for cold-spots within the target volume
- Serial cost function: Limitation of the high-dose exposure of OAR and prevention of the functionality-loss of a single sub-unit
- Parallel cost function: Limitation of the intermediate-dose exposure of a wide range of volume and prevention of the functionality-loss of a certain percentage of sub-units

Biological cost functions are based on the equivalent uniform dose (EUD)-concept. The EUD-concept assumes the equality of a homogeneous and an inhomogeneous dose distribution causing the same radio-biological effect [62].

$$D_{EUD} = \left(\frac{\sum_{i=1}^N v_i D_i^k}{\sum_{i=1}^N v_i} \right)^{\frac{1}{k}} \quad (2.1)$$

The parameter k represents tissue-specific quantity for biological cost functions and its reaction to a certain dose.

The most commonly used cost functions for the treatment plans in this study were the Target-EUD, the quadratic overdose and the serial cost function, which are described below.

Target-EUD: The Target-EUD cost function is based on the linear quadratic model and describes the cell kill/ cell survival of the tumor cells. For homogeneous tumor cell density the function is given by:

$$f(D_{(x)}) = \rho e^{-\alpha D_{(x)}} \quad (2.2)$$

$D_{(x)}$ represents the dose at a certain point x , ρ the relative cell density and α the cell sensitivity. Target-EUD is based on the minimization of the low-dose voxels to increase the cell deaths[63]. The effective tumor dose is given by:

$$D_{eff} = -\frac{1}{\alpha} \ln \frac{\sum_{i=1}^N \rho e^{-\alpha D(x_i)}}{\sum_{i=1}^N v_i} \quad (2.3)$$

Quadratic overdose: Applied in conjunction with the Target-EUD, the quadratic overdose function can reduce high doses in the PTV in order to avoid hot-spots. It can also be used for OAR to shape the dose gradient along the PTV. The function is calculated by:

$$g(D_{(x)}) = \Theta(D_{(x)} - D_C)(D_{(x)} - D_C)^2 \quad (2.4)$$

$\Theta(D_{(x)} - D_C)$ represents the heaviside function and D_C a certain reference dose, which defines a threshold for a voxel. Below this threshold the quadratic dose function is zero. But if the dose exceeds the threshold, the function becomes the quadratic difference according to 2.4.

The effective dose is given by:

$$D_{eff} = \sqrt{\frac{\sum_{i=1}^N \Theta(D(x_i) - D_C)(D(x_i) - D_C)^2}{N}} \quad (2.5)$$

This dose is constrained depending on the overdose acceptance.

Serial cost function: Anatomical structures whose functionalities depend on linked sub-units must be protected against the loss of a single one. Thus, the maximum of the

dose must be minimized. Correspondingly, many points on the DVH with emphasis on high doses must be controlled.

The penalty of each voxel x is given by:

$$g(D_{(x)}) = \left(\frac{D_{(x)}}{D_C} \right)^k \quad (2.6)$$

The penalty depends on the height of parameter k . Resulting from this dependency, the exposure of the OAR to high doses decreases with an increasing parameter k . This is shown in Figure 2.3.

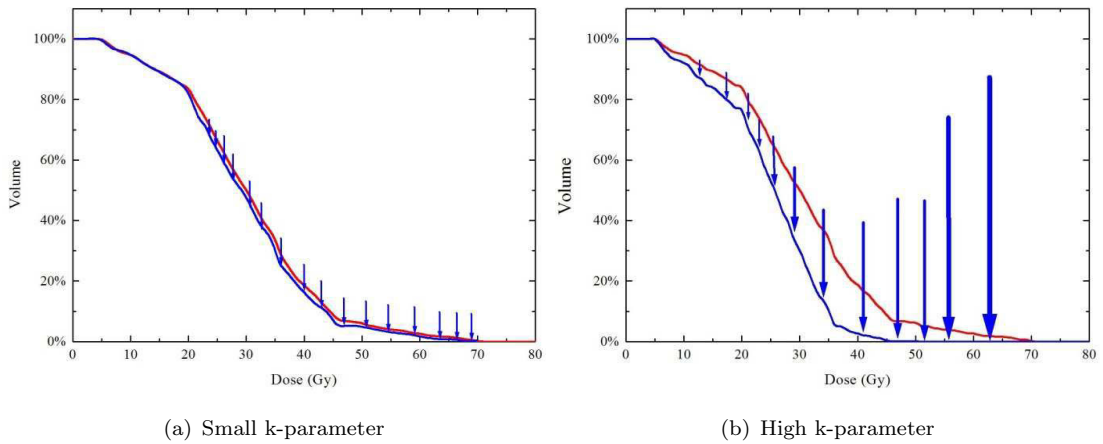


FIGURE 2.3: Influence of the k - parameter on the DVH of a serial organ[63]

Parallel cost function: Parallel cost functions are related to anatomical structures, which tolerate high dose values in small subunits if the rest is spared. This cost function effects the entire DVH-curve in varying degrees and particularly works in the middle of the DVH curve 2.4. Thus, many points on the DVH with emphasis on the mean dose must be controlled and minimized.

2.3.1.2 Treatment plan configuration

A very important issue regarding the configurations of treatment plans was the attempt to find optimal beam angles. This was done under the conditions to fulfil an adequate dose coverage of at least 95% of the $PTV_{initial}$ and the PTV_{boost} with 95% of the prescribed dose, combined with a low dose exposure of the primary organs at risk.

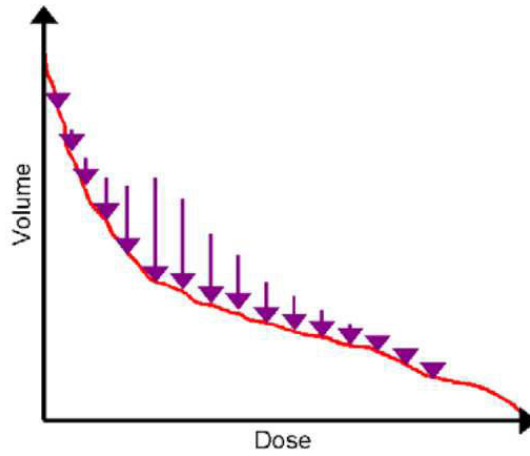


FIGURE 2.4: Influence on the DVH of a parallel organ[63]

Correspondingly, a fundamental consideration of the localization of the PTV and OAR within the PTV has to be done during the planning process.

For the treatment of $PTV_{initial}$ six photon beams from the ipsilateral to cranio-caudal direction had proven to fulfil this prerequisite. In contrast to the $PTV_{initial}$, only four beams were used for the treatment of PTV_{boost} because of the smaller volume, which was easier to cover.

The beam angles were consistent for all patients depending on the localisation of the tumor in the left or right brain hemisphere. Table 2.7 shows the beam configuration of the 6 beams for the initial plans. The first 4 beams represent the configuration for the boost plans.

Tumor in left brain hemisphere			Tumor in right brain hemisphere	
Beam	Gantry	Couch	Gantry	Couch
1	270°	0°	90°	0°
2	260°	90°	240°	90°
3	300°	90°	280°	90°
4	290°	60°	70°	300°
5	280°	90°	260°	90°
6	280°	40°	80°	320°

TABLE 2.7: Beam configuration of patients with the tumor localized in the left or right brain hemisphere. All 6 beams were used to treat PTV_{init} and only the first 4 to treat PTV_{Boost} .

Furthermore, an appropriate amount of segmentations were taken into account. The number of segmentations had to exceed 30. The grid size of the dose calculation matrix was reduced from $4 \times 4 \times 4 \text{ mm}^3$ to $2 \times 2 \times 2 \text{ mm}^3$ for the final plans.

2.3.2 XiO

In this study the treatment planning software XiO V.4.4.1 (Elekta, CMS software, Crawley, UK) was used for spot scanning with IMPT. For dose calculation and optimisation the pencil beam algorithm was used. An inverse planning approach is used, where a computer-based optimization process weights each spot and performs a pencil beam weight optimization. In this optimization the number of protons associated with each pencil beam is adjusted in order to find an optimal solution for the prescribed dose for the PTV and to spare OAR [64].

Basically, the optimization scheme can be described as:

$$\text{minimize : } f(d(x)), \text{ where : } x \geq 0 \quad (2.7)$$

x represents the vector of pencil beam weights, d the vector dose and f the total cost function. d results from the sum of dose vectors associated with each pencil beam.

In contrast to the Monaco system the XiO is only based on physical constraints for PTV and the anatomical structures like OAR. For the target volume it is restricted on the input of a maximum, a minimum dose and a goal for the aimed dose including weighting factors. For the OAR individual dose-volume points can be set in order to minimize the dose exposure and the dose maximum of the OAR during the optimization process. The optimization process ends when the cost function converges to the solution or when a certain number of iterations is exceeded [65].

2.3.2.1 Treatment plan configuration

In contrast to the IMXT beam setting, the search for an adequate beam configuration has to be done individually for each patient for IMPT plans. Resulting from that, the beam configuration process was very time consuming in order to obtain an appropriate solution, which fulfils the prerequisites regarding the PTV coverage and the less OAR exposure to radiation.

For the PTV_{initial}, two beams were applied from the ipsilateral direction. As a consequence of the fixed beam lines for protons, which was assumed, the gantry angle was fixed at 270° and only the couch angles were varied. In contrast to the PTV_{initial}, two beams were applied from the cranio-caudal direction for the PTV_{boost}, in order to obtain

separate entrance regions for the four beams used in the entire treatment. The different beam directions are illustrated in Figure 2.5.

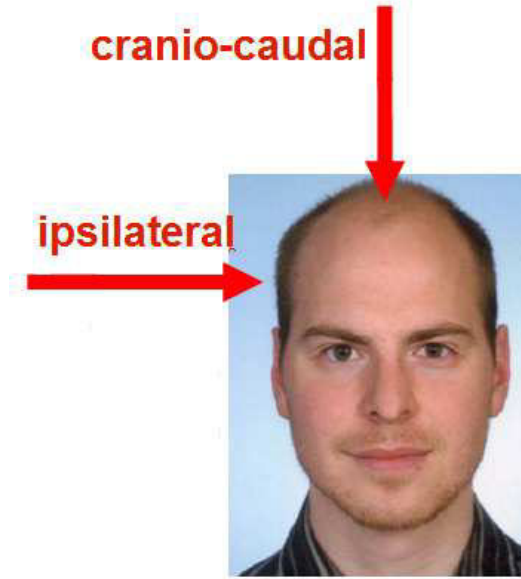


FIGURE 2.5: Beam directions for $PTV_{initial}$ and PTV_{boost}

The individually obtained beam settings for the $PTV_{initial}$ and PTV_{boost} for each patient are shown in table 2.8.

	$PTV_{initial}$		PTV_{boost}	
	Beam 1	Beam 2	Beam 1	Beam 2
MA 1	0°	20°	90°	70°
MA 2	20°	50°	80°	100°
MA 4	10°	340°	90°	70°
MA 6	20°	50°	90°	70°
MA 7	10°	350°	80°	60°
MA 8	170°	200°	100°	80°
MA 9	160°	180°	100°	80°
MA 10	20°	350°	90°	70°
MA 11	180°	160°	110°	130°
MA 12	180°	160°	100°	80°

TABLE 2.8: Couch angle configurations for the $PTV_{initial}$ and PTV_{boost} for each patient

The two beams for the respective treatment plan were always separated by a couch angle of 20° to 30°. For the $PTV_{initial}$, couch angles ranging from -30° and 30° with regard to the horizontal beam line were investigated and the best beam positions were chosen. For the PTV_{boost} , beam positions along the cranio-caudal beam line were taken into account.

Additionally, XiO was capable of applying range shifters for superficially localized tumors, in order to obtain a good PTV coverage. Moreover, help structures were created for the limitation of maximum dose. Thus, high doses were suppressed in order to avoid "hot-spots" in normal tissue.

Another important issue for the beam configuration is the number of spots in the target, which is, for example, determined by the distance of the spot layers or geometrical parameters defining the lateral space between individual Bragg peaks. The number of spots during the optimization process corresponds to the degrees of freedom and to the ability to create individual dose distributions for each patients. Furthermore, the distance of the dose spots has to be low, in order not to influence the homogeneity of the dose distribution [41].

In this study, the spacing between the IMPT energy layers was 0.8 cm, the spot size (FWHM) 0.3 cm and the distance between spots was 0.5 cm [41].

Furthermore, the grid size of the dose calculation matrix was reduced from $4 \times 4 \times 4 \text{ mm}^3$ to $2 \times 2 \times 2 \text{ mm}^3$ for the final plans, in order to avoid fluctuations of inhomogeneous proton dose distribution. For some created plans only a grid size of 0.3 was obtainable, due to the limited computational capacities.

2.3.3 TRiP

For carbon ions, the treatment planning system TRiP98 V.1001c, which was developed at the GSI, was used. It was designed to cooperate with three dimensional active dose shaping devices like the GSI raster scanning system. In order to describe the interactions of the carbon ion beams with the human tissue, both a physical and a biological model are implemented in the TRiP 98 treatment planning system [66, 67, 68].

The used TriP98 version provides three different algorithms for dose calculation, the classic, the allpoints and the multiscatter algorithm, which are described in detail in the publications by Michael Krämer [66, 67]. The fastest algorithm for the calculation of the dose on the CT grid is the "classic" approach, where 4 neighboring raster points are taken into account for each voxel. Contrarily, the "allpoints" algorithm considers all neighboring raster beams spots. When using multiple field optimization as is was done in this study the "allpoints" algorithm is recommended because it provides a more accurate dose calculation. The multiscatter algorithm additionally accounts for the broadening of each beams spot as function of depth. It was not used in this study, since the accuracy of the "allpoints" algorithm was sufficient.

Since charged particles like carbon ions are high LET radiation, they have an enhanced RBE compared to protons. The incorporation into a treatment planning system is not trivial, since the RBE depends nonlinearly on the atomic number of the tissue, the absorbed dose and particles energy. Different models for the calculation of the RBE are discussed in the particle community. The model used TRiP98 is the local effect model LEM [69, 70].

To receive the biological effective dose, the physical dose is multiplied by the local RBE factors calculated using the LEM model according the formula 2.8.

$$D = D_{bio} = D_{phys} \times RBE(dN(E_{beam,z,Z,E})(dE)) \quad (2.8)$$

The calculation algorithms used in the TRiP98 TPS are based on the assumption of water equivalent targets. To account for density variation on the CT the concept of the water equivalent path length (WEPL) is included. The conversion of hounsfield units (HU) into WEPL is based on the experimental data which are explained in the publications [71, 72, 73].

2.3.3.1 Treatment plan configuration

As for the proton plans only a fixed beam from horizontal direction was assumed and the couch angle was varied to treat the PTV_{init} from ipsilateral and the PTV_{Boost} from cranio-caudal direction. In contrast to proton plans, the coordinate system was defined differently. While for the proton beams the gantry angle was fixed at 270°, the gantry angle was fixed at 0° for the carbon ions. Correspondingly, also the couch angles were varied according to the shifted coordinate system. The two coordinate systems with their differently defined gantry (g) and couch (c) angles are illustrated in Figure 2.6.

The chosen configurations for all patients according to the TRiP98 coordinate system are listed in table 2.9.

The couch angles were chosen in the same way as for the proton treatment plans with the aim to receive the best possible isodose distribution with respect to target coverage and OAR sparing. Following this strategy, different couch angles were chosen for proton and carbon ion plans for some patients with a couch angle separation between the two beams of 20° or 30°. For all treatment plans a calculation spot size (FWHM) of 4-6 mm was used in combination with a Bragg peak width of 3 mm.

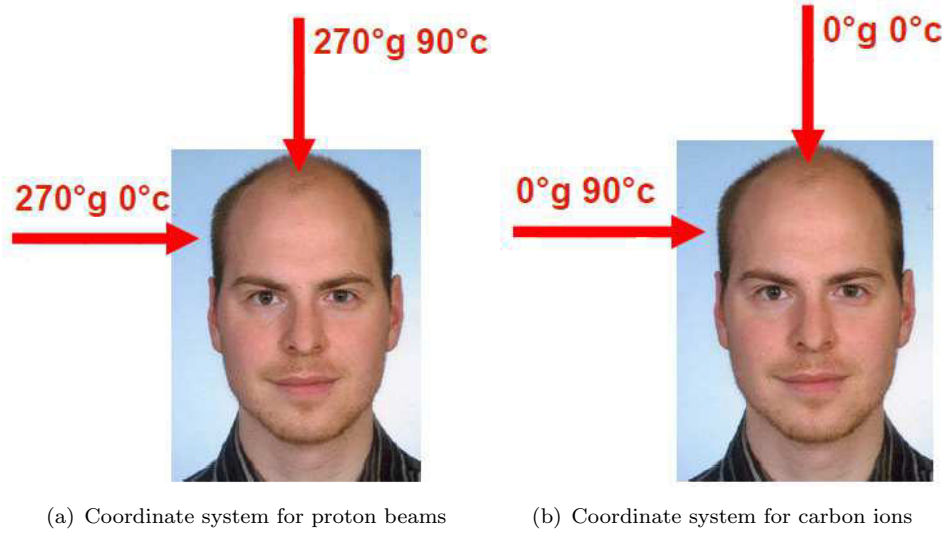


FIGURE 2.6: Definitions of gantry (g) and couch (c) angles for proton and carbon ion therapy in the present study

	PTV _{initial}		PTV _{boost}	
	Beam 1	Beam 2	Beam 1	Beam 2
MA1	80°	100°	0°	20°
MA2	70°	90°	0°	20°
MA4	80°	100°	0°	20°
MA6	80°	110°	-10°	20°
MA7	80°	100°	-10°	20°
MA8	-80°	-100°	-10°	10°
MA9	-80°	-100°	-30°	0°
MA10	80°	100°	0°	20°
MA11	-80°	-100°	0°	-20°
MA12	-80°	-100°	0°	-20°

TABLE 2.9: Couch angle configurations for the PTV_{initial} and PTV_{boost} for each patient

2.4 CERR

With the MATLAB based software platform CERR (V.4.1) the dose matrices of the initial plans and the boost plans were summed up on a voxel by voxel basis. Furthermore, an in-house developed MATLAB based software tool (MathWorks, Natick, Massachusetts (USA) R2009, 64 bit) was used to create patient averaged dose-volume-histograms and to assess dosimetric differences between plans and plan combinations.

CERR (Version 4.1, May 2012) [74] is a Matlab-based Computational Environment for Radiation Research. CERR is capable of importing and displaying treatment plans from a wide variety of commercial or academic treatment planning systems, if the data is available in the DICOM format. CT-imaging systems and treatment planning systems

2.5.1 DVH Export

After the creation of DVHs by CERR, a txt-output file for the chosen DVHs including five columns can be exported, using a Matlab command. Each column represents either a cumulative DVH with absolute values, a differential DVH or a cumulative weighted DVH concerning the dose or the volume.

2.5.2 Dosimetric parameters

For the evaluation of the DVHs, various dosimetric parameter were of interest to assess the quality of the treatment plans in means of PTV coverage and OAR sparing.

2.5.2.1 Dose-volume-parameters

The "dose-volume"-parameters represent the deposited dose [Gy(RBE)] at a certain percentage of volume of a target volume or a OAR. For this study the following "dose-volume"-parameters, recommended by the ICRU83 [46], were used for evaluations of the PTVs and the organs at risk:

- Dose [Gy(RBE)] at 2% of volume ($D_{2\%}$) as surrogate for maximum dose
- Dose [Gy(RBE)] at 50% of volume ($D_{50\%}$) as surrogate for median dose
- Dose [Gy(RBE)] at 95% of volume ($D_{95\%}$) as surrogate for dose coverage
- Dose [Gy(RBE)] at 98% of volume ($D_{98\%}$) as surrogate for minimum dose

To illustrate the developed Matlab based software tool, one basic function in form of the "dose-volume"-parameter is given below in terms of the Matlab-code including comments. This function is capable of calculating any volume at a certain dose. This was done for the volumes listed above.

In order to avoid redundancy this type of Matlab-code documentation is performed once for this representative function only. The following documentation is dealing with the "DoseAtVol"-function and the function parameters "DVH" and "VolValue".

Code for the function to calculate dose at volumes

```
function Dose=DoseAtVol(DVH, VolValue)
%This function delivers a dose at a certain volume from a DVH. It searches for the closest volume value
%and interpolates between the two closest points.

Range=5; % size of search pattern
Dose=-1; % set a default dose, which can be recognized as error state.
curpos=0;

% calculate the closest of all values to the VolValue according to the position
[min_diff,pos]=min(abs(DVH(:,2)-VolValue));

if (min_diff < Range)
    tmpDose(1)=DVH(pos,1);
    tmpVol(1)=DVH(pos,2);
    sizeOfDVH=size(DVH);

    % finding the parameters for interpolation
    if (sizeOfDVH(1) == pos) %only if the last value is the searched one
        % safety check, to prevent failure on empty volumes
        if (tmpVol(1)==0)
            Dose=0;
        else %(tmpVol(1)==0)
            % find the temp doses for interpolation
            tmpDose(1)=DVH(pos-1,1);
            tmpDose(2)=DVH(pos,1);
            tmpVol(1)=DVH(pos-1,2);
            tmpVol(2)=DVH(pos,2);

            % if the last value is higher the the wanted one, create a value and then interpolate
            if (DVH(pos,2)>VolValue)
                tmpDose(1)=DVH(pos,1);
                intv=DVH(2,1)-DVH(1,1);
                tmpDose(2)=tmpDose(1)+intv;
                tmpVol(1)=DVH(pos,2);
                tmpVol(2)=0;
            end % (DVH(pos,2)>VolValue)
        end % (tmpVol(1)==0)

    % here if the searched value is not at the boundaries
    else % (sizeOfDVH(1) == pos)

        % if the closest value is lower than the searches value
        if (DVH(pos,2)<VolValue)
            ch=1; curpos=pos;

            % the first dose value is per definition zero, and so is the dose
            if (pos==1)
                Dose=0;
            else % (pos==1)
                % that only happens if more equal points are the closest to VolValue,
                %so we pick just the last one
                while(ch==1)
                    tmpDose(2)=DVH(curpos-1,1);
                    tmpVol(2)=DVH(curpos-1,2);
                    if (tmpVol(2)>VolValue) ch=0;
                end
            end
        end
    end
end
```

```

        else curpos=curpos-1;
        end % (tmpVol(2)>VolValue)
    end % (ch==1)
end % (pos==1)

% if the closest value is higher than the searches value
else % (DVH(pos,2)<VolValue)
    ch=1; curpos=pos;
    % that only happens if more equal points are the closest to VolValue,
    % so we pick just the last one ;
    % and make sure the index does not exceed matrix dimensions
    while(ch==1 && curpos < length(DVH))
        tmpDose(2)=DVH(curpos+1,1);
        tmpVol(2)=DVH(curpos+1,2);
        if (tmpVol(2)<VolValue) ch=0;
        else % (tmpVol(2)<VolValue)
            curpos=curpos+1;
            tmpDose(1)=DVH(curpos,1);
            end % (Vol(2)<VolValue)
        end % while(ch==1 && curpos < length(DVH))
    end % if (DVH(pos,2)<VolValue)
end % (sizeOfDVH(1) == pos)

% check existence of parameter and do the interpolation
if (Dose ~= 0 && curpos ~= length(DVH))
    Dose=interp1(tmpVol,tmpDose,VolValue);
elseif (curpos == length(DVH))
    Dose=tmpDose(1);
end % (Dose ~= 0 && curpos ~= length(DVH))

else % (min_diff < Range)
    Dose=0;
end % (min_diff < Range)

```

Another type of "dose-volume"-parameters represent a certain amount of volume [%] which is exposed to a certain percentage of dose. For the evaluation the parameters at 20% of dose ($V_{20\%}$), at 50% of dose ($V_{50\%}$), at 80% of dose ($V_{80\%}$) and at 95% of dose ($V_{95\%}$) were used.

2.5.2.2 Mean dose

The mean dose (D_{mean}) is defined as the sum of the product of voxel doses D_i divided by the number of voxels n :

$$D_{mean} = \frac{\sum_{i=1}^n D_i}{n} \quad (2.9)$$

2.5.2.3 Homogeneity index

The homogeneity index (HI) represents the steepness of the curve in a PTV-DVH and characterizes the tendency of the fall-off. The HI is defined by ICRU83 [46] as follows:

$$HI = \frac{D_{2\%} - D_{98\%}}{D_{50\%}} \quad (2.10)$$

$D_{50\%}$ represents the normalization value.

The closer the HI is to zero, the higher is the indication of a nearly homogeneous dose distribution.

2.5.2.4 Conformity index

The conformity index (CI) represents the quotient of the treated volume and the planning target volume. The CI, defined by Paddick et al [75], describes to what extent the volume of a dose distribution conforms to the size and the shape of a target volume.

$$CI = \frac{TVPI^2}{PI * TV} \quad (2.11)$$

TVPI is the PTV subvolume encompassed by the 95% isodose, PI the volume of 95% isodose and TV the total planning target volume. Thus, an ideal conformity corresponds to a CI-value of 1.

2.5.3 Statistical evaluation

In order to obtain assessments over all 10 patients, statistical evaluations including Student's t-test were performed.

2.5.3.1 Mean value and standard deviation

Firstly, the mean value \bar{X} over all patients of every dosimetric parameter was determined by ([76], p.413):

$$\bar{X} = \frac{X_1 + X_2 + \dots + X_N}{N} = \frac{\sum_{i=1}^N X_i}{N} \quad (2.12)$$

X_i represents a dosimetric parameter for a certain patient and N the number of patients.

Secondly, the standard deviation of the mean value S was ([76], p.413):

$$S = \sqrt{\frac{\sum_{i=1}^N V_i^2}{N-1}} = \sqrt{\frac{\sum_{i=1}^N (X_i - \bar{X})^2}{N-1}} \quad (2.13)$$

V_i represents the deviation of the dosimetric parameters X_i to the mean value \bar{X} , if $N \geq 2$.

2.5.3.2 Student's t-test

Finally, all dosimetric parameters for both PTVs and the OARs were compared by performing the paired two tailed student's t-test ([76], p.416ff).

$$t = \frac{\bar{X} - \mu_0}{\frac{S}{N}} \quad (2.14)$$

As given in formula 2.14, the paired t-test proves for two depending samples, if the unknown mean value μ is equal to the presumed mean value μ_0 . \bar{X} is therefore the assuming-function for μ . The null hypothesis is $\mu = \mu_0$. A prerequisite is the normal distribution of the differences.

The standards for the comparison were either the IMXT plans for the PTV-comparison or the combined IMXT_{initial}+IMXT_{boost} plans for the OAR-comparison. The results from the Student's t-test were assumed as significant for a p-level ≤ 0.05 .

2.5.4 Operating instructions for the evaluation software

Corresponding to the three evaluation chapters above, the evaluation process can be performed by three main scripts of the in-house developed Matlab-software tool in this order:

- The script "DVHExport" exports txt-outcome files from a certain Matlab-readable CERR-file.
- The script "calculateIndices" calculates all parameters described above for a certain patient.
- The script "calculateStatistics" performs the statistical evaluation in order to create patient averaged dose-volume-histograms with the related parameters and their statistical characteristics.

All of the scripts can be activated by the "Run"-command in the Matlab-environment.

Chapter 3

Results

The aim of the following chapter is to provide and discuss the results of this study. As outlined earlier, the three treatment modalities were intensity modulated photon therapy (IMXT), intensity modulated proton therapy (IMPT) and carbon ion therapy (^{12}C).

In order to obtain a systematic structure, the chapter is divided into two main parts:

- Target volumes
- Organs at risk

3.1 Target volumes

In this chapter the results for both the single and the combined plans are presented for the planning target volume (PTV). The illustration of the target coverage is done by means of dose-volume histograms and the characterisation by various parameters, which were introduced in chapter 2.6.2.

3.1.1 Initial and boost plans

In Figure 3.1 and 3.2 the dose distribution of the initial and boost plans of IMXT, IMPT and ^{12}C are illustrated for a representative patient. Differences regarding the medium and the low dose levels and the sharpness of the penumbra between IMXT and the light ion modalities can be observed.

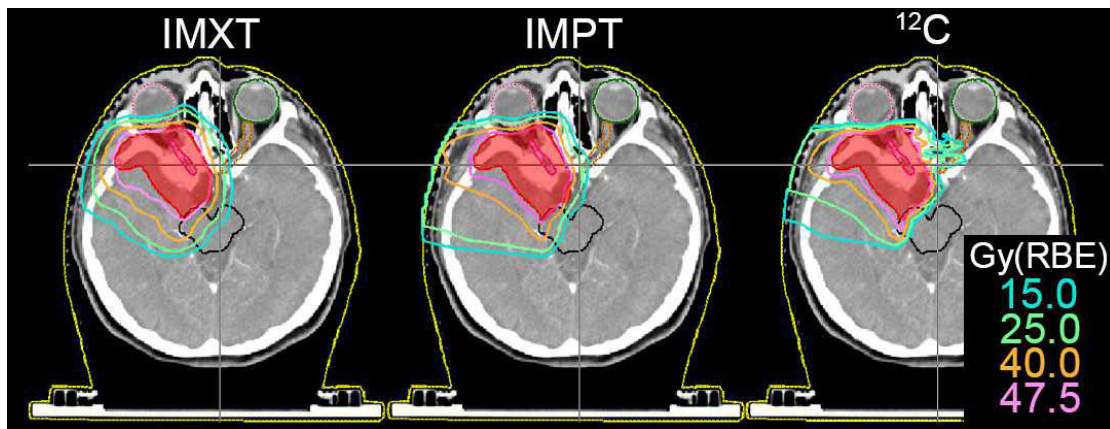


FIGURE 3.1: Dose distribution of PTV_{init}

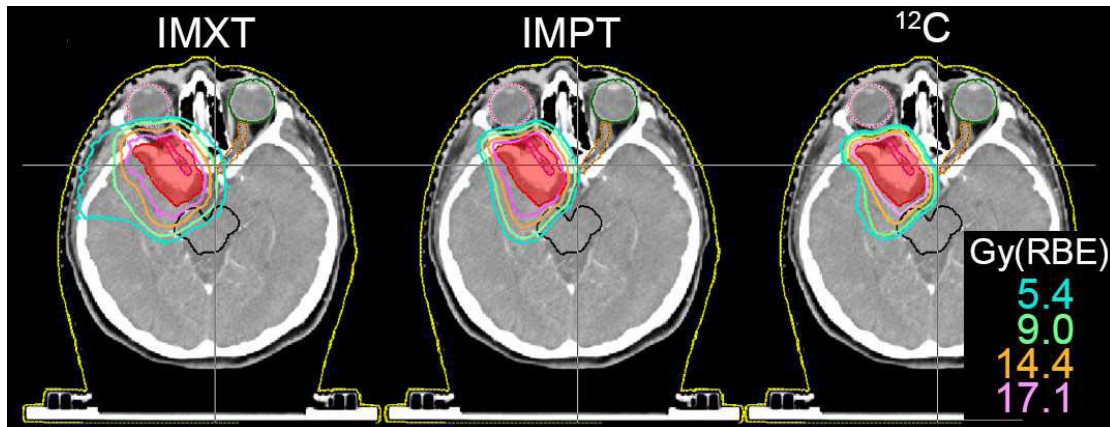
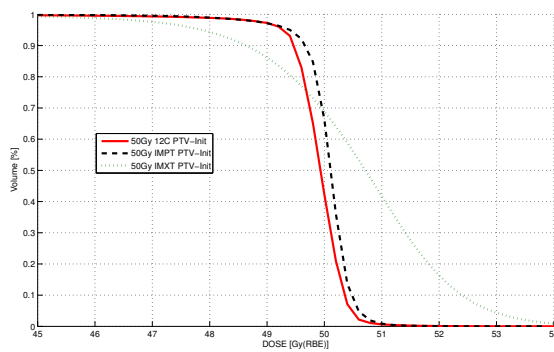
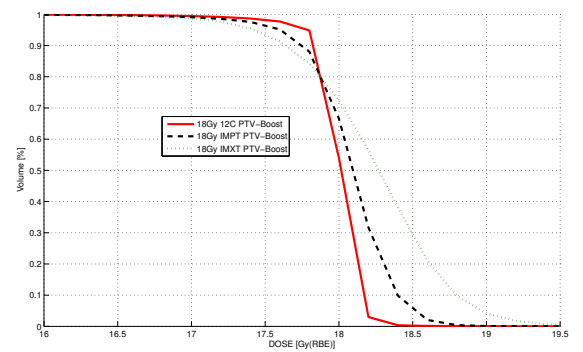


FIGURE 3.2: Dose distribution of PTV_{boost}



(a) DVH of PTV_{init}



(b) DVH of PTV_{boost}

FIGURE 3.3: DVHs of PTVs

Similar to the resulting dose distributions in Figure 3.1 and 3.2, the DVH of both the PTV_{init} and the PTV_{Boost} of the three treatment techniques are depicted in Figure 3.3.

The graph of IMXT declines first and exceeds the prescribed dose for both PTVs the most. Moreover, IMXT reveals the worst dose coverage across the target volume and the highest maximum dose $D_{2\%}$. However, none of the treatments exceeded the maximal tolerated dose of 107% according to [46] and thus, unwanted "hot-spots" in healthy tissue were avoided.

In contrast to IMXT, the IMPT and ^{12}C dose volume histograms for the PTVs showed a similar behaviour in terms of dose maximum and decline. Both reveal a better coverage and a reduced high dose level.

Tables 3.1 and 3.2 provide selected important average dosimetric parameters of PTV_{init} and PTV_{Boost} . All values were compared with respect to the results obtained for IMXT using the Student's t-test. Significant differences ($p \leq 0.05$) are indicated with S in the tables 3.1 and 3.2.

PTV_Initial								
	IMXT		IMPT			12C		
	Mean value	Standard deviation	Mean value	Standard deviation	p	Mean value	Standard deviation	p
D 2% [Gy(RBE)]	53.36	0.56	50.77	0.20	S	50.64	0.08	S
D 50% [Gy(RBE)]	50.72	0.23	50.11	0.08	S	49.93	0.11	S
D 98% [Gy(RBE)]	46.69	0.77	48.71	0.36	S	48.62	0.59	S
V 95% [%]	96.08	1.34	99.29	0.35	S	99.11	0.54	S
HI	0.13	0.02	0.04	0.01	S	0.04	0.01	S
CI	0.57	0.03	0.73	0.05	S	0.81	0.05	S

TABLE 3.1: Average dosimetric parameters of PTV_{init} with mean values and standard deviation and the significant differences (depicted by S)

PTV_Boost								
	IMXT		IMPT			12C		
	Mean value	Standard deviation	Mean value	Standard deviation	p	Mean value	Standard deviation	p
D 2% [Gy(RBE)]	19.11	0.23	18.59	0.12	S	18.26	0.06	S
D 50% [Gy(RBE)]	18.27	0.10	18.10	0.06	S	18.01	0.04	S
D 98% [Gy(RBE)]	17.16	0.32	17.31	0.12		17.54	0.12	S
V 95% [%]	97.64	2.01	98.58	0.56		99.17	0.34	S
HI	0.11	0.02	0.07	0.01	S	0.04	0.01	S
CI	0.44	0.07	0.69	0.04	S	0.78	0.03	S

TABLE 3.2: Average dosimetric parameters of PTV_{boost} with mean values and standard deviation and the significant differences (depicted by S)

The median dose $D_{50\%}$ fulfilled the prescribed dose of 50 Gy(RBE) and 18 Gy(RBE) within a range less than 1.5% for PTV_{init} and PTV_{Boost} , respectively.

The maximum dose was represented by the parameter $D_{2\%}$. IMXT indicated the highest $D_{2\%}$ values for both PTVs. Concerning the PTV_{init} of the IMXT plans, $D_{2\%}$ was 53.36 Gy(RBE). When compared to the IMPT and ^{12}C plans, the maximum dose of IMXT is almost 3 Gy(RBE) higher than the light ion modalities. Whereas the maximum dose of IMPT is only slightly higher than ^{12}C . Moreover, the boost plans showed similar tendencies.

The dosimetric parameter which characterizes the decline and the steepness of the graph is the homogeneity index (HI) and was calculated according to ICRU83 [46]. The HI was described in chapter 2.5.2.3.

IMXT had the highest HI value with 0.13 and 0.11 for both the initial plans and the boost plans, respectively. This underlined the observations in Figure 3.3 in terms of the highest dose maximum and the most progressive decline of the IMXT graph, when compared to IMPT and ^{12}C . The HI of the light ion modalities was approximately 0.04, whereas ^{12}C revealed the best homogeneity concerning the boost plans.

The dosimetric parameter $V_{95\%}$ represents the dose coverage of a certain amount of volume at 95% of the prescribed dose.

However, $V_{95\%}$ was higher than 95% for all of the treatment modalities, i.e. all plans were fulfilling the dose prescription. IMXT revealed lower values than IMPT and ^{12}C . Thus, a higher dose coverage was obtained using particle therapy modalities. Particularly, $V_{95\%}$ of the initial plans ranged from 96.05 % for IMXT to more than 99.1 % for the light ion plans. The values of IMPT and ^{12}C were comparable high. Concerning the boost plans, ^{12}C was even 0.6 % superior to IMPT. Otherwise, the results were comparable for boost and initial plans.

In order to assess the conformity of the dose distribution across the target volume and the shape of the penumbra, the conformity index (CI) was calculated according to Paddick et al [75] as described in chapter 2.5.2.4. The CI describes to what extent the volume of a dose distribution conforms to the size and the shape of a target volume. A high conformity index indicates a close surrounding of the target volume resulting to a lower exposure of the normal tissue to the 95 % isodose level. In this regard, the light ion treatment modalities were superior to IMXT. ^{12}C revealed the highest CI with 0.81 for the initial treatment plans. This was higher by almost 0.25, when compared to IMXT, which had a CI of 0.57. Concerning the boost plans, the difference between the CI of IMXT and ^{12}C was even more than 0.3. The IMPT plans indicated also a higher CI than IMXT, but ^{12}C revealed the best results for both plans. The slightly superior conformity of ^{12}C over IMPT can be explained by the less lateral scattering and the sharper shape of the Bragg peak of carbon ions as depicted in Figure 1.

All parameters for the initial plans of IMPT and ^{12}C yielded a significant difference (depicted by S), when compared to the parameters of IMXT. The parameter of the boost plans were consistent to those of the initial plans.

3.1.2 Combined plans

The PTVs of the combined treatment plans IMXT+IMXT, IMPT+IMPT and $^{12}\text{C}+^{12}\text{C}$ with a total prescribed dose of 68 [Gy(RBE)] of a representative patient are shown in Figure 3.4.

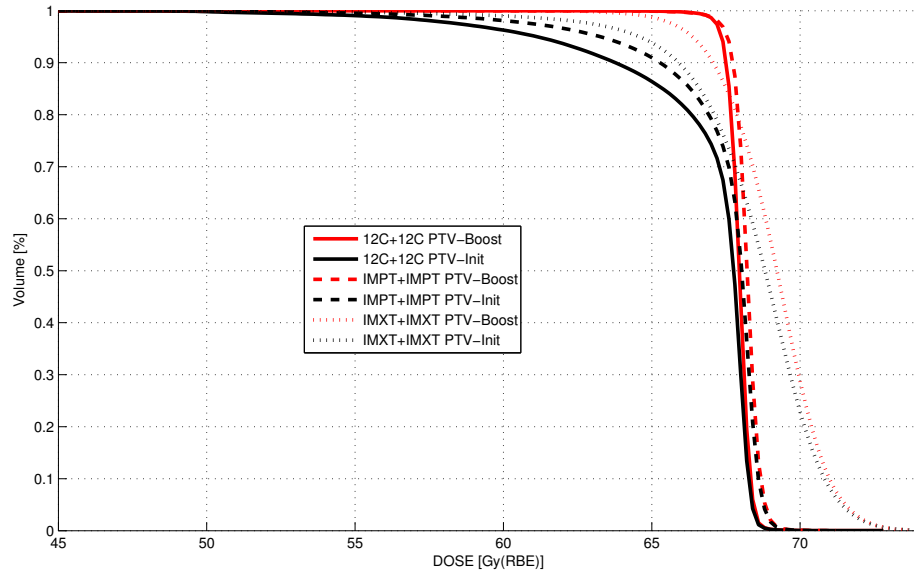


FIGURE 3.4: DVH of the combined plans

As it can be seen in Figure 3.4, $^{12}\text{C}+^{12}\text{C}$ revealed the closest surrounding of the 64.6 Gy(RBE) (95% of 68Gy(RBE)) isodose around the boost PTV, which led to a lower dose for the initial volume. This is illustrated in Figure 3.4 by the rapid decline of the initial graph of $^{12}\text{C}+^{12}\text{C}$. The conformity and the dose distribution are depicted in Figure 3.5.

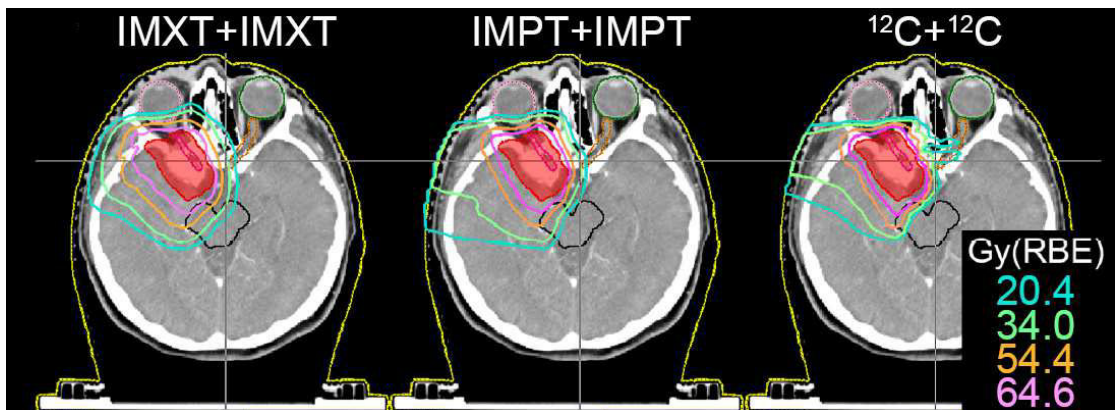


FIGURE 3.5: Dose distribution of combined plans

It can easily be seen, that the penumbra of the light ion treatments is much sharper. Also the extent of the low dose levels is more focused around the target volume and less healthy tissue is exposed to radiation.

Nevertheless, a more extended low dose level at the entrance areas was observed for the proton and carbon ion plans than for the IMXT treatment plans. This is caused by the number of beams which were used for the treatment. Resulting from the smaller number of fixed beams coming from the same direction and being separated by small couch angles only, the entrance areas for IMPT and ^{12}C showed a different dose distribution than IMXT.

The comparison of the entrance areas of IMPT and ^{12}C showed a reduced dose extent for ^{12}C .

3.2 Organs at risk (OAR)

This chapter is related to the evaluation of the dose exposure of organs at risk. For this study the OAR were divided in two groups, as described in chapter 2.2.2:

- Primary OAR
- Secondary OAR

The primary OAR contained organs which were considered during the optimization process. This group contained organs of the optical pathway as well as large areas of the brain.

The secondary OAR included smaller organs in the surrounding of the target volume and anatomical structures as the whole brain hemisphere.

A summary of the averaged dosimetric parameters $D_{2\%}$, $D_{50\%}$, D_{mean} , $V_{20\%}$, $V_{50\%}$, $V_{80\%}$ for selected primary OARs is given in Tables 5.1 and 5.2 in the appendix. Tables 5.3 and 5.4 contain the parameters for selected secondary OARs.

3.2.1 Primary OAR

3.2.1.1 Eyes

In Figure 3.6 the DVHs of both the eye_i and the eye_c are shown for the combinations of sole photon, carbon ion and proton treatments.

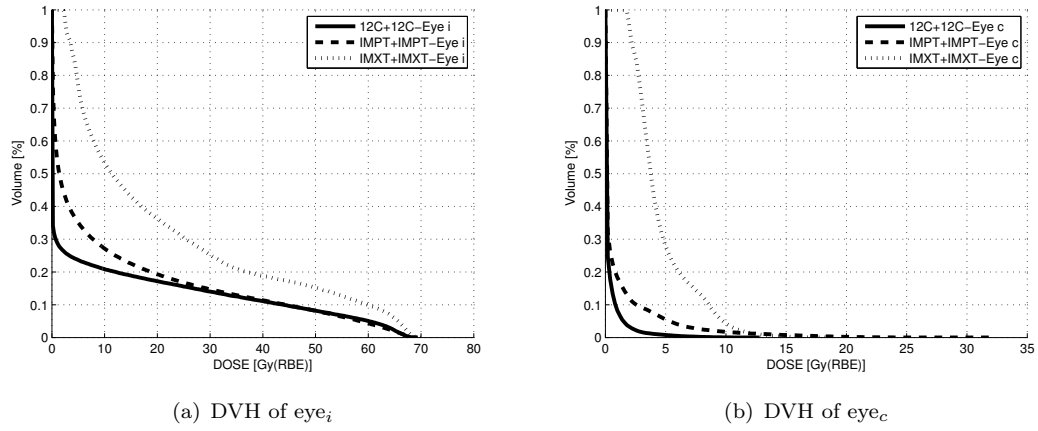


FIGURE 3.6: DVHs of eyes

Both the IMPT+IMPT and the $^{12}\text{C}+^{12}\text{C}$ modalities showed a sparing of the eyes compared to IMXT+IMXT. $D_{2\%}$, $D_{50\%}$ and D_{mean} revealed a significant difference for all of the compared modalities. The maximum dose $D_{2\%}$ of the eye_c was 8.2 Gy(RBE) for the IMXT+IMXT modality and was reduced using the $^{12}\text{C}+^{12}\text{C}$ modality by almost 7 Gy(RBE). The mean dose of the eye_c declined for these modalities from 4.5 Gy(RBE) to approximately 0 Gy(RBE). For the eye_i , $D_{2\%}$ was reduced from 38.6 Gy(RBE) down to 20.6 Gy(RBE), which corresponded to a decrease by even 18 Gy(RBE). The mean dose decreased from 20.8 Gy(RBE) to 9.0 Gy(RBE).

Concerning the dosimetric parameter $V_{20\%}$, the eye_c was reduced to no dose exposure at all and $V_{20\%}$ of the ipsilateral eye was reduced from 45.5 % to 19.4 %, when $^{12}\text{C}+^{12}\text{C}$ was compared to IMXT+IMXT.

Also the mixed-combined modalities combining IMXT as initial plan with ^{12}C and IMPT as boost treatment revealed a significant enhanced sparing in terms of $D_{2\%}$, $D_{50\%}$ and D_{mean} , when compared to IMXT+IMXT. Particularly, $D_{2\%}$ of the eye_i decreased to 33.7 Gy(RBE) for the IMXT+ ^{12}C modality, which corresponded to a dose reduction of almost 5 Gy(RBE). Nevertheless, the sole carbon and proton modalities were superior.

The reason for these achievements in terms of dose reduction is the close locations of the PTV next to the eye_i without including the eye itself. Only for two patients the PTV reached partly into the eye's volume. Consequently, a sharper penumbra and a better conformation had an impact on the reduction of the middle and low dose areas and so on the dose exposure of the eyes.

The dose limits of former studies were according to chapter 2.2.2:

- $\text{eye } D_{mean} < 6.1 \text{ Gy(RBE)}$

- eye $V_{35} < 50 \text{ Gy(RBE)}$
- lens $D_{2\%} < 6 \text{ Gy(RBE)}$

The dose constraint for the parameter V_{35} was always fulfilled for both eyes. The D_{mean} -limit of 6.1 Gy(RBE) was fulfilled only for the eye_c. The dose exposure of the eye_i is that high due to the localization at the edge of the PTV.

The maximal dose limit of 6 Gy(RBE) was always fulfilled for the lens_c. For the lens_i, the $D_{2\%}$ -limit is only fulfilled for the sole carbon and proton combinations, due to the reduced extent of the low and medium dose distribution.

3.2.1.2 Optical pathway

The optical pathway consists of both optical nerves, optical nerves_c and optical nerves_i, and the chiasm. The DVHs of the optical pathway for the combinations of sole photon, carbon ion and proton treatments are shown in Figures 3.7 and 3.8.

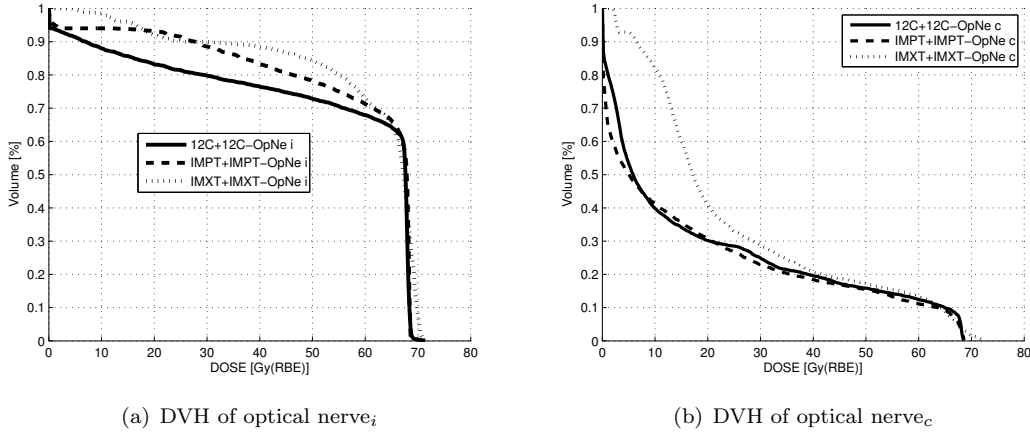


FIGURE 3.7: DVHs of optical nerves

The dosimetric parameters $D_{2\%}$, D_{mean} and $V_{20\%}$ of the contralateral optical nerve revealed significant differences for every treatment modality when compared to IMXT+IMXT. This behaviour was comparable the eyes, although the dose reduction were not that pronounced. In particular, the dose maximum was reduced from 43.8 Gy(RBE) to 37.3 Gy(RBE), when $^{12}\text{C}+^{12}\text{C}$ was compared to IMXT+IMXT. Since a large part of the contralateral optical nerve was included in the PTV for two patients, the standard deviation of the mean values was quite high. Nevertheless, significant differences were observed comparing IMXT+IMXT with the particle beam modalities for most dosimetric parameters, as depicted in Table 5.1 and 5.2 in the appendix.

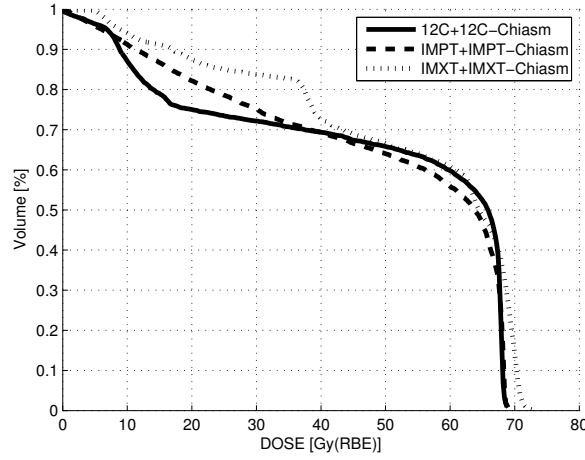


FIGURE 3.8: DVH of chiasm

On the contrary, the optical nerve_i revealed barely significances for the comparison of most of the dosimetric parameters. Moreover, dose sparing was difficult because the ipsilateral optical nerve was almost totally included within the PTV for most of the patients. Consequently, the optical nerve_i could hardly be included into the optimization process.

However, only the $^{12}\text{C}+^{12}\text{C}$ modality obtained a significant dose reductions in terms of the parameters $D_{2\%}$ and D_{mean} . $D_{2\%}$ decreased from 65.5 Gy(RBE) to 64.2 Gy(RBE) and D_{mean} from 59.6 Gy(RBE) to 53.3 Gy(RBE).

The dose limit of former studies were according to chapter 2.2.2:

- optical nerve $D_{2\%} < 60$ Gy(RBE)

The optical nerve_c fulfilled always the dose limit. Contrarily, due to the localization within the PTV, the optical nerve_i did never.

The comparison of the dosimetric parameters of the chiasm, which is the connection between the optical nerves, did not reveal significant differences independent of the compared treatment modalities. This resulted from the small size and the location of the chiasm. In eight of ten patients the chiasm was located completely within the PTV and thus, the optimization process was not possible at all.

The dose limit of former studies were according to chapter 2.2.2:

- chiasm $D_{mean} < 54$ Gy(RBE)

- chiasm $D_{2\%} < 60 \text{ Gy(RBE)}$

The average D_{mean} value of the chiasm fulfilled the limit of 54 Gy(RBE) for all modalities. Nevertheless, for five patients this limit was exceeded by more 10 Gy(RBE), for two it was exceeded slightly and only for three patients the chiasm was completely outside of the PTV. Resulting from that, the chiasma could only be involved into the optimization process for three patients. For the other patients an elevated risk existed to become blind, according to the high dose exposure of the chiasm.

The maximum dose limit of 60 Gy(RBE) was not fulfilled of any modality at all.

3.2.1.3 Brainstem and cerebellum

The DVHs of both the brainstem and the cerebellum for the combinations of sole photon, carbon ion and proton treatments are depicted in Figure 3.9.

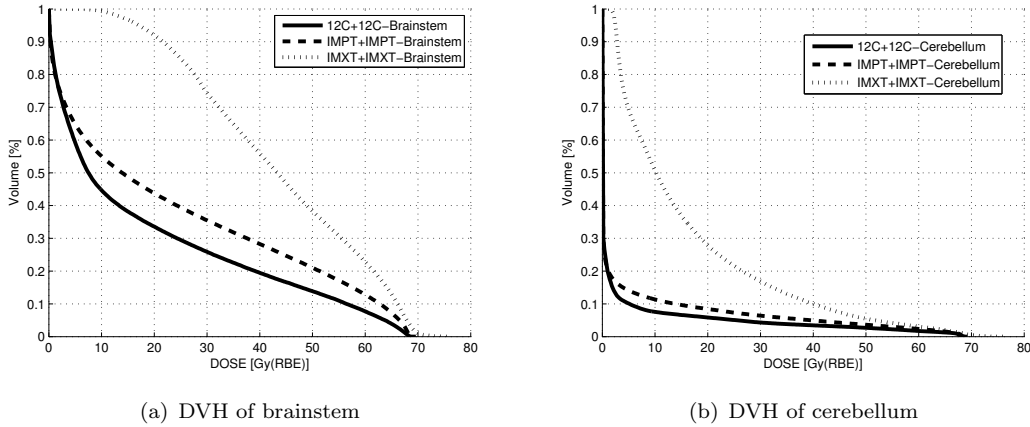


FIGURE 3.9: DVHs of brainstem and cerebellum

The comparison of all chosen dosimetric parameters of the brainstem revealed a significant difference for every treatment modality, when compared to IMXT+IMXT. The results of the evaluation of the dosimetric parameters of the cerebellum were almost consistent to the brainstem in terms of significant differences.

When $^{12}\text{C}+^{12}\text{C}$ was compared to IMXT+IMXT, the mean dose decreased from 43.5 Gy(RBE) to 18.3 Gy(RBE) for the brainstem and from 16.0 Gy(RBE) to 3.4 Gy(RBE) for the cerebellum, respectively. Moreover, the dose maximum $D_{2\%}$ revealed a reduction from 66.8 Gy(RBE) to 61.6 Gy(RBE) for the brainstem and from 53.9 Gy(RBE) to 34.1 Gy(RBE) for the cerebellum, respectively. Also the parameter $V_{20\%}$ and $V_{50\%}$ illustrated the dose reduction. $V_{20\%}$ decreased from 97.7 % to 39.7 % for the brainstem and from 40.2 % to 6.9 % for the cerebellum, respectively. $V_{50\%}$ was reduced from

66.7 % to even 23.2 % for the brainstem and from 13.8 % to 3.9 % for the cerebellum, respectively.

The PTV was located closely to the brainstem and the cerebellum, but did hardly reach into their volumes and thus, a higher conformity with the target volume had an impact on the dose exposure of the brainstem and the cerebellum.

The dose limit of former studies were according to chapter 2.2.2:

- brainstem $D_{mean} < 53 \text{ Gy(RBE)}$

This dose limit could be fulfilled for all treatment modalities and combinations.

3.2.1.4 Pituitary gland

In Figure 3.10 the DVHs of the pituitary gland (hypophysis) is depicted for the combinations of sole photon, carbon ion and proton treatments.

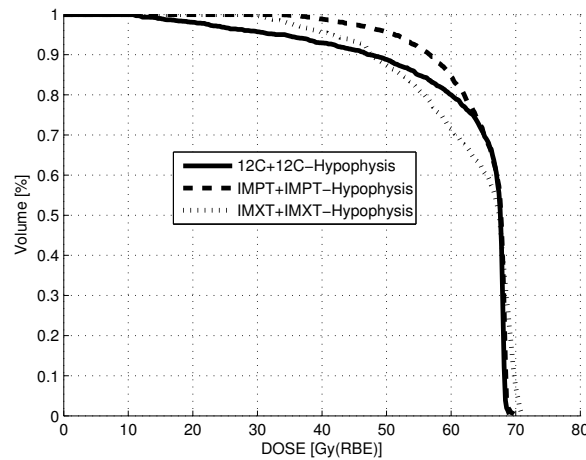


FIGURE 3.10: DVH of hypophysis

Due to the localisation and the small size, the results of the pituitary gland were comparable to them of the chiasm. No significant differences for any treatment modality or any dosimetric parameter were observed at all. Since the pituitary gland was located completely within the PTV for eight patients, the optimization process was hardly possible.

The dose limit of former studies were according to chapter 2.2.2:

- pituitary gland $D_2 < 50 \text{ Gy(RBE)}$

This dose limit was not fulfilled for any treatment modality. The limit was exceeded by more than 12 Gy(RBE) caused by the inclusion within the PTV for most of the patients.

3.2.1.5 Comparison of mixed modalities for selected primary OAR

The DVH curves of sole and mixed treatment combinations for selected primary OAR are compared in Figure 3.11.

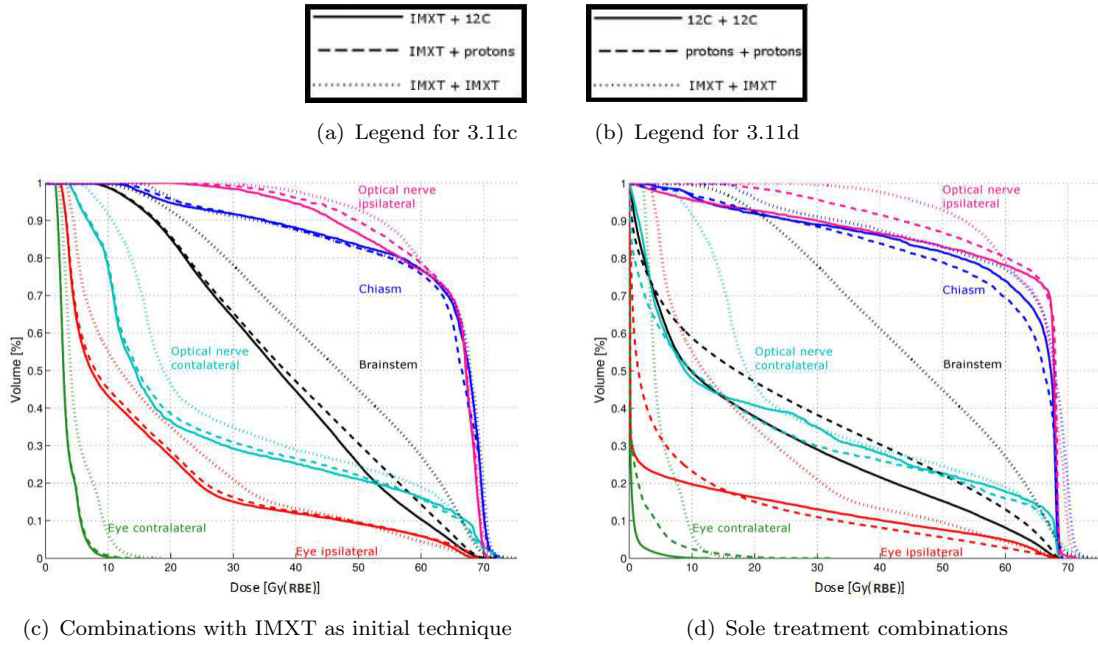


FIGURE 3.11: Comparison of sole and mixed treatment combinations for various primary OARs

As shown in Figure 3.11c, the dose exposure of organs at risks varies with the boost modality, when IMXT is chosen as treatment technique for $PTV_{initial}$. Particularly, with carbon ion boost a dose reduction was obtained. The mean dose of the eye_i and the brainstem decreased from 20.8 Gy(RBE) to 17.4 Gy(RBE) and from 43.5 Gy(RBE) to 36.4 Gy(RBE), respectively. The benefits of carbon ion boosts were already described by Combs et al [53] with the study "MARCIE Trial" at die HIT in Heidelberg in terms of the progression-free survival rate as the primary endpoint and the overall survival, safety and toxicity as secondary endpoints.

However, the organ at risk sparing of the modalities with IMXT as initial technique was not that pronounced as it was with of sole treatment combinations, as illustrated in Figure 3.11d. Here, the mean dose of the eye_i and the brainstem decreased from 20.8 Gy(RBE) to 9.0 Gy(RBE) and from 43.5 Gy(RBE) to 18.3 Gy(RBE), respectively. Particularly, the dose sparing of the brainstem with the sole carbon modality is remarkable. When $^{12}C + ^{12}C$ was compared to IMXT+IMXT, the volume exposed to dose were

reduced for the parameters $V_{20\%}$, $V_{50\%}$ and $V_{80\%}$ from 97.7 % to 39.7 %, from 66.7 % to 23.2 % and from 31.7 % to 11.4 %.

For OARs with a high percentage of their volume within the PTV like the optical nerve_i and the chiasm, a high dose sparing could not be observed using different boost modalities.

3.2.2 Secondary OAR

3.2.2.1 Brain hemisphere

The brain hemisphere is an anatomical structure, which expands the ipsilateral and the contralateral brain areas, called brain_c and brain_i. In Figure 3.12 the DVHs of both hemispheres are shown for the combinations of sole photon, carbon ion and proton treatments, respectively.

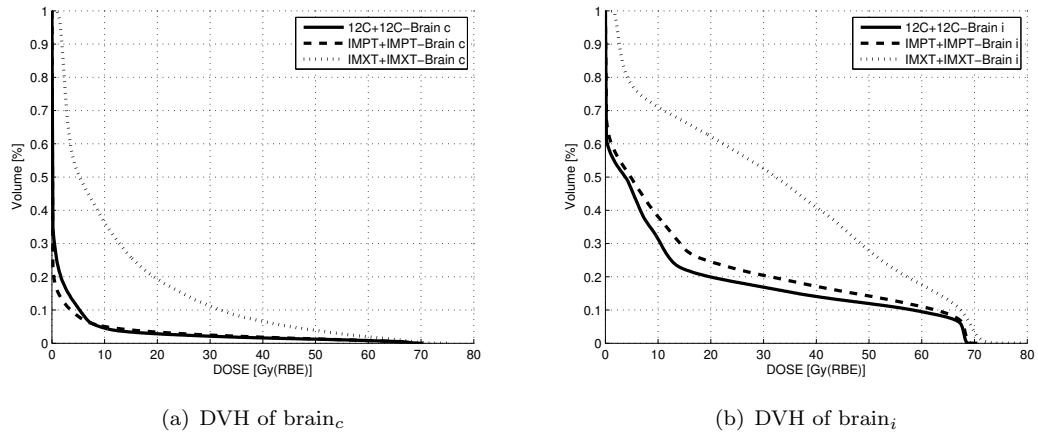


FIGURE 3.12: DVH of brain hemispheres

The brain_c, which is an important indicator for dose of the normal tissue on the contralateral side of the brain, revealed significant differences for all dosimetric parameters of the sole carbon ion and proton modalities, when compared to IMXT+IMXT. Particularly with the $^{12}\text{C} + ^{12}\text{C}$ combination, the parameter $D_{2\%}$ was reduced from 51.4 Gy(RBE) to 30.3 Gy(RBE) and $V_{20\%}$ from 28.4 % to 3.6 %. For the mean dose and the parameter $V_{50\%}$ even the IMPT+IMPT modality was superior to $^{12}\text{C} + ^{12}\text{C}$. This is probably resulting from the fragmentation tail of the carbon ions, which extends from the distal edge of the tumor to the contralateral brain hemisphere and causes dose exposure.

Concerning the ipsilateral brain, the carbon ion modality was superior to both the photons and the protons and had similar significant differences as brain_c. However, this

differences had to be considered with caution, because the ipsilateral brain hemisphere is almost spared for one patient and thus, the averaged values were influenced.

3.2.2.2 Secondary contralateral OAR

A special focus was put on the organs at risk on the contralateral side to obtain comparable indicators for the dose distribution in normal tissue. In Figure 3.13 DVH curves of selected secondary contralateral OAR are illustrated. These OAR are the cochlea_c, the hippocampus_c and hypothalamus_c.

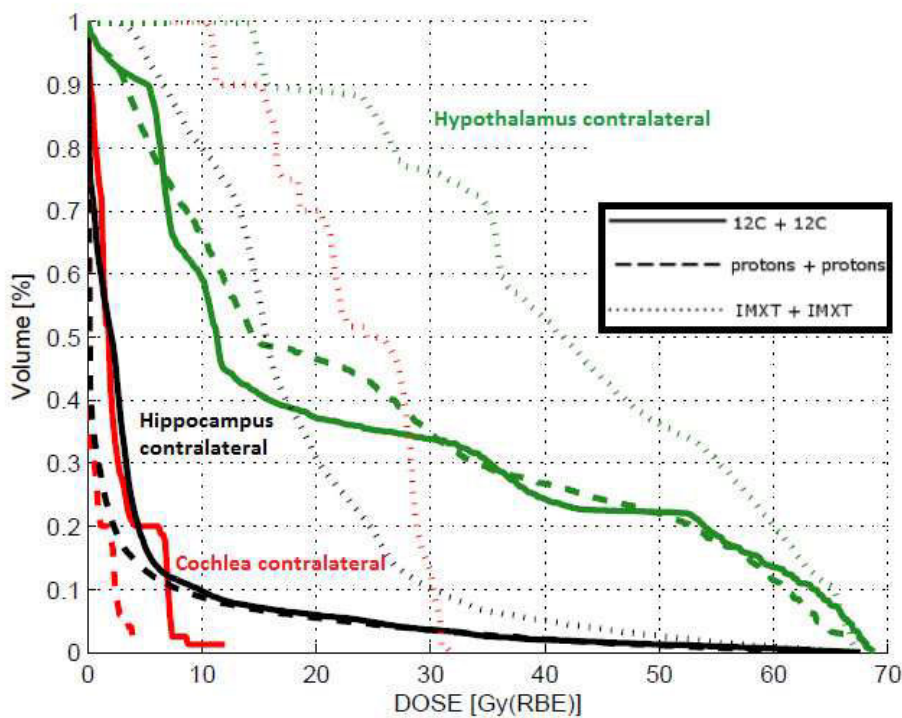


FIGURE 3.13: DVH of cochlea_c, hippocampus_c and hypothalamus_c

For light ion therapy a high dose reduction for contralateral secondary organs was observed, even if these organs were not directly included in the optimization process. Particularly, the mean dose of the cochlea_c and the hippocampus_c were reduced from 23.1 Gy(RBE) and 18.0 Gy(RBE) to below 5 Gy(RBE) with the light ion modalities, respectively. Furthermore, the parameter $V_{20\%}$ decreased from 90 % to zero for the cochlea_c and from 68.1 % to approximately 7 % for the hippocampus_c. Moreover, all "Dose-volume"-parameters of the proton and carbon ion treatment plans were significantly reduced, when compared to IMXT-IMXT.

Concerning the hypothalamus_c, dosimetric parameters $D_{2\%}$, D_{mean} and $V_{20\%}$ revealed significant differences. When $^{12}C + ^{12}C$ was compared to IMXT+IMXT, $D_{2\%}$ was reduced from 49.3 Gy(RBE) to 35.2 Gy(RBE), D_{mean} from 42.6 Gy(RBE) to 23.8 Gy(RBE) and $V_{20\%}$ from 99.7 % to 42.5 %.

The IMPT+IMPT modality was even slightly lower as $^{12}C + ^{12}C$ in terms of the dose maximum and the mean dose. The cochlea_c even revealed significant differences, when the proton modality was compared to the carbon ion modality. This resulted again from the fragmentation tail of the carbon ions.

The dose limit for the cochlea of former studies were according to chapter 2.2.2:

- cochlea $D_{mean} < 45.1$ Gy(RBE)

This limit was for the cochlea_c always fulfilled due to less dose exposure at the contralateral side.

3.2.2.3 Secondary ipsilateral OAR

In Figure 3.14 various DVHs of the ipsilateral OARs are illustrated.

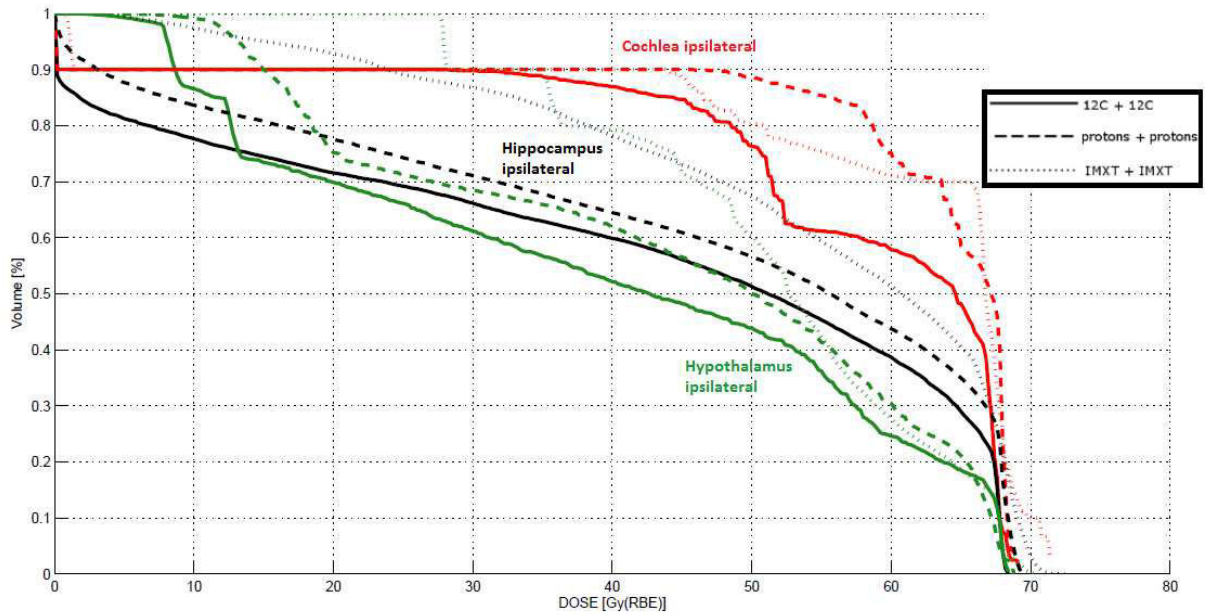


FIGURE 3.14: DVH of cochlea_i, hippocampus_i and hypothalamus_i

These OAR indicated a high exposure to radiation, depending on the amount of their volume within the PTV.

However, the hippocampus_i and the hypothalamus_i revealed a significant dose reduction of the mean dose by more than 10 Gy(RBE) with the carbon ion modality. On the other hand, the cochlea_i revealed no significance for any dosimetric parameter. And thus, the dose limit of former studies according to chapter 2.2.2 of $D_{mean} < 45.1$ Gy(RBE) was not fulfilled for any modality.

Chapter 4

Summary and Outlook

The aim of this study was to compare the dosimetric characteristics of photon, proton and carbon ion therapy and to combine their different characteristics in order to obtain the most beneficial treatment technique for atypical or malignant skull base meningioma patients.

The coverage of the target volumes were excellent for all treatment modalities. Light ion beam therapy, however, was superior to photon therapy in certain aspects. The target coverage was improved and furthermore a higher grade of target conformity and target dose homogeneity was obtained and the total integral dose was reduced. IMPT and ^{12}C revealed similar characteristics in terms of the planning target volume, though for ^{12}C slightly better plan evaluation parameters were obtained. This might arise from the better coverage of carbon ions, due to the sharper shape of the Bragg peak and the less lateral scattering. Kosaki et al [77] obtained similar results with a higher target dose conformity and a better OAR sparing for the carbon ion plans, when compared with the proton and photon plans. They also used horizontal beams for the light ion beam therapy as in this present study and concluded that the IMPT and ^{12}C have the potential to overcome the lack of gantry for skull base meningioma. Nevertheless, Kosaki et al included only 5 patients in their study, where the application of a non-gantry plan could be approved. In our study acceptable plans using no gantry could be achieved for all ten patients considered in our study.

Concerning the primary OARs, light ion beam therapy revealed a high dose reduction to the normal tissue and a sparing of most of the considered organs. This was revealed by organs localized in the vicinity of the PTV (Figures 3.6 and 3.9). In particular, for both the brainstem and the cerebellum the dose exposure to low dose areas decreased rapidly in proton and carbon ion treatment plans. Concerning the sparing of the eyes and the brainstem results presented by Kosaki et al [77] were consistent with our study.

Furthermore, mixed modality combinations revealed promising results compared to the IMXT+IMXT option. As shown in Figure 3.11c, the dose exposure of organs at risks was reduced, when light ion boosts were used in combination with IMXT as the initial technique. Particularly, with the carbon ion boost a dose reduction was obtained for the brainstem, the eyes and the optical nerve_c. The "MARCIE Trial" study by Combs et al [53] investigates the benefits of carbon ion boosts in combination with photon radiotherapy in terms of the progression-free survival rate as the primary endpoint and the overall survival, safety and toxicity as secondary endpoints at HIT in Heidelberg. The clinical study started in the year 2010. However, it was shown in Figure 3.11b, that the combination of sole treatments with protons and carbon ions was superior to the combinations with IMXT as initial treatment in terms of the primary OAR sparing. Consequently, the present study and other comparisons of light ion beam and IMXT irradiation favour the use of sole particle therapy approaches [78, 79].

Additionally, the light ion treatment plans revealed to be superior to IMXT in terms of secondary contralateral organs (3.13). In more detail, IMPT showed even slightly better results than ^{12}C , when the "Dose at Volume"-parameters were compared. This might be resulting from the fragmentation tail of the carbon ions, which caused higher doses at the distal edge of the tumor extending to the contralateral hemisphere of the brain. All of the "Dose at Volume"-parameters revealed statistical significances and an improved dose sparing. The anatomical structure of the contralateral brain hemisphere confirmed this assumption due to the less integral dose of IMPT, when compared with ^{12}C (3.12a).

On the contrary, the high dose treatment of atypical or malignant skull base meningiomas was associated with a high dose exposure to the optical pathway and probably related to a significant risk of side effects [80]. This concerned organs of which a large extent of their volume are located within the PTV, such as the ipsilateral optical nerves and the chiasm (3.7a and 3.8). They revealed relatively equal doses in all treatment techniques with no significant difference.

The results of the pituitary gland were similar to the chiasm as a consequence of the comparable localized anatomical vicinity to the PTV (3.10).

In 2010, Combs et al [81] initiated a study about carbon ion therapy for high-risk meningiomas. In this study ^{12}C was conjuncted with fractionated stereotactic radiation therapy and IMXT in order to perform dose escalation with more than 60 Gy(RBE). The aim was to obtain a control of the local tumor recurrences due to a high conformity and homogeneity of the target volume with carbon ion therapy. Additionally, a reduction of the integral dose in normal tissue to reduce long term side effects was expected. Both, the increased control rates and the integral dose reduction had already been demonstrated in

previous studies [82, 83, 84, 85]. Combs et al treated 8 patients with ^{12}C in conjunction with IMXT as primary radiation therapy and 2 patients as re-irradiation. The carbon ion therapy was applied with a median dose of 18 Gy(RBE) and IMXT with 50.4 Gy(RBE). The two former irradiated patients received a reduced IMXT dose. After the primary radiation therapy an actuarial local control of 72% at 5 years and 58% at 7 years were obtained. The 2 re-irradiated patients developed tumor recurrences at 10 and 67 months after the treatment [81]. In Figure 4.1 the tumor control is illustrated by the progression-free survival in the 10 patients.

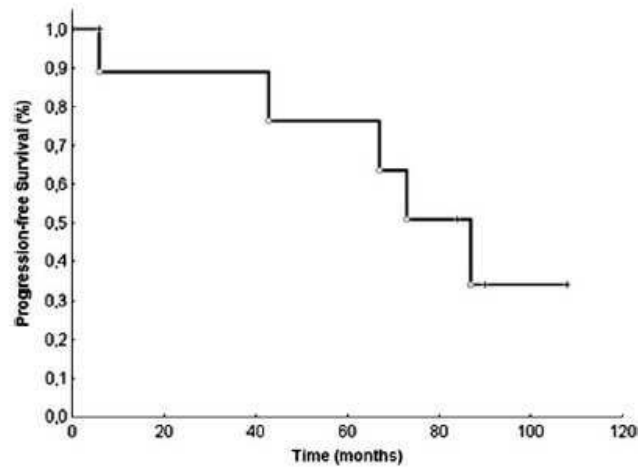


FIGURE 4.1: Progression-free survival curve [81]

The promising results from the Combs study are complementary to the results of the present study and the superior characteristics of ^{12}C , when compared to IMXT and particularly IMPT contributes to further considerations concerning the application of ion beam therapy in clinical studies.

Additionally, it is important to note that in the present study the beam arrangements of particle beam therapy plans were limited to a horizontal beam delivery. The focus of a horizontal beam line only was motivated by the fact that no gantry will be available in the start up phase of the MedAustron facility. Nevertheless, high PTV coverage and good OAR sparing were obtained using carbon ions or protons for the treatment. A gantry system would enable additional degrees of freedom and possibly lead further improvement due to the higher flexibility to radiate even difficult localized anatomical regions [86, 77]. However, the realization of a gantry for light ion therapy bears several difficulties, for example, a more complex search for the optimal beam configuration. But particularly, if the tumor extends mainly along the beam directions, the benefits could be significant, when compared with fixed horizontal beam delivery systems [77]. Consequently, a gantry for light ions would be a promising consideration to replace fixed particle beam lines in the future. Many gantries for proton therapy are already existing,

but for carbon ion therapy only one gantry exists at the HIT in Heidelberg. Solving technical challenges like the massive construction and geometrical aspects which are needed to be considered to realize a carbon ion therapy with a rotating gantry device are the tasks for the next years.

Chapter 5

Appendix

		D 2% [Gy(RBE)]		p	D 50% [Gy(RBE)]		p	D mean [Gy(RBE)]		p
		Mean value	Standard deviation		Mean value	Standard deviation		Mean value	Standard deviation	
Eye c	IMXT+IMXT	8.19	3.63		4.22	2.09		4.47	2.19	
	IMXT+IMPT	5.99	2.69	S	2.91	1.10	S	3.10	1.24	S
	IMXT+12C	5.76	2.34	S	2.89	1.08	S	3.05	1.18	S
	IMPT+IMPT	3.17	6.25	S	0.73	1.58	S	0.89	1.99	S
	12C+12C	1.34	2.46	S	0.25	0.27	S	0.27	0.48	S
Eye i	IMXT+IMXT	38.61	20.63		19.66	22.01		20.77	19.77	
	IMXT+IMPT	35.61	21.35	S	16.56	21.21	S	17.90	19.14	S
	IMXT+12C	33.71	21.50	S	16.39	21.33	S	17.42	19.18	S
	IMPT+IMPT	30.10	24.78	S	9.40	16.66	S	10.85	15.06	S
	12C+12C	20.64	28.35	S	8.51	17.58	S	8.98	16.22	S
Brainstem	IMXT+IMXT	66.79	4.60		43.77	11.04		43.47	8.78	
	IMXT+IMPT	64.85	4.27	S	36.85	9.24	S	37.86	7.77	S
	IMXT+12Ca	63.53	5.26	S	35.24	8.28	S	36.40	7.36	S
	IMPT+IMPT	63.83	5.08	S	19.27	17.74	S	23.49	12.57	S
	12C+12C	61.57	7.47	S	11.74	10.42	S	18.29	9.63	S
Cerebellum	IMXT+IMXT	53.90	15.28		11.35	7.26		16.00	8.07	
	IMXT+IMPT	50.23	16.48	S	8.38	5.14	S	12.82	6.22	S
	IMXT+12C	47.64	16.79	S	8.39	5.21	S	12.59	6.24	S
	IMPT+IMPT	43.45	23.46	S	0.16	0.06	S	4.64	4.27	S
	12C+12C	34.09	26.85	S	0.35	0.48	S	3.37	3.71	S
Optical Nerve c	IMXT+IMXT	43.77	23.75		24.93	19.27		25.31	16.02	
	IMXT+IMPT	41.86	23.49	S	21.79	20.28	S	22.26	16.39	S
	IMXT+12C	41.43	24.49	S	21.76	20.53	S	21.81	15.93	S
	IMPT+IMPT	39.88	22.05	S	15.59	25.54	S	17.23	19.56	S
	12C+12C	37.27	25.70	S	18.80	25.89	S	18.13	19.40	S
Optical Nerve i	IMXT+IMXT	65.53	14.54		61.91	16.26		59.63	15.88	
	IMXT+IMPT	65.83	12.75		61.36	17.21		58.89	15.94	
	IMXT+12C	65.40	13.51		60.52	17.62		57.83	16.27	S
	IMPT+IMPT	65.90	8.26		59.90	20.95		57.41	16.45	
	12C+12C	64.16	14.49	S	57.35	21.57		53.25	19.46	S
Chiasm	IMXT+IMXT	62.01	16.82		54.47	21.35		53.49	20.07	
	IMXT+IMPT	63.82	14.02		54.43	19.27		53.34	18.19	
	IMXT+12C	63.61	14.41		55.04	19.28		53.74	18.25	
	IMPT+IMPT	64.38	8.67		51.21	22.21		49.73	20.19	
	12C+12C	60.83	15.87		52.07	23.80		49.09	22.58	
Hypophyse	IMXT+IMXT	67.98	3.83		63.28	7.73		62.45	7.99	
	IMXT+IMPT	68.72	2.63		63.97	6.28		63.00	6.69	
	IMXT+12C	68.66	2.65		63.67	6.55		62.73	7.06	
	IMPT+IMPT	68.53	0.68		65.82	3.27		64.66	4.26	
	12C+12C	67.99	1.24		64.21	7.05		62.23	8.80	

TABLE 5.1: Averaged dosimetric parameters $D_{2\%}$, $D_{50\%}$, D_{mean} for selected primary OAR and the significant differences (depicted by S)

		V 20% [%]		p	V 50% [%]		p	V 80% [%]		p
		Mean value	Standard deviation		Mean value	Standard deviation		Mean value	Standard deviation	
Eye c	IMXT+IMXT	0.63	1.73		0.00	0.00		0.00	0.00	
	IMXT+IMPT	0.02	0.07		0.00	0.00		0.00	0.00	
	IMXT+12C	0.00	0.00		0.00	0.00		0.00	0.00	
	IMPT+IMPT	1.01	3.19		0.00	0.00		0.00	0.00	
	12C+12C	0.00	0.00		0.00	0.00		0.00	0.00	
Eye i	IMXT+IMXT	45.54	35.33		21.59	38.02		13.05	27.98	
	IMXT+IMPT	38.91	41.40		19.62	37.50		10.56	22.17	
	IMXT+12C	37.66	42.05	S	18.92	37.39		10.61	22.37	
	IMPT+IMPT	23.62	32.56	S	13.27	24.30		6.57	13.39	
	12C+12C	19.38	33.85	S	12.76	25.04		6.91	15.47	
Brainstem	IMXT+IMXT	97.65	3.16		66.73	19.82		31.69	20.42	
	IMXT+IMPT	95.16	5.41	S	54.25	19.59	S	20.79	14.24	S
	IMXT+12Ca	94.95	5.56	S	51.75	19.96	S	15.91	12.33	S
	IMPT+IMPT	50.36	23.63	S	32.55	20.57	S	17.61	15.11	S
	12C+12C	39.68	20.39	S	23.18	15.20	S	11.37	10.09	S
Cerebellum	IMXT+IMXT	40.16	23.35		13.79	11.27		4.30	4.69	
	IMXT+IMPT	31.39	18.84	S	8.67	7.01	S	3.21	3.90	S
	IMXT+12C	31.26	18.97	S	8.29	7.06	S	2.54	3.51	S
	IMPT+IMPT	10.07	8.66	S	5.78	5.99	S	3.07	3.96	
	12C+12C	6.85	7.00	S	3.91	4.56	S	2.30	3.31	S
Optical Nerve c	IMXT+IMXT	67.08	27.92		25.35	31.85		15.60	24.49	
	IMXT+IMPT	50.45	30.10	S	21.96	30.72	S	13.77	24.27	
	IMXT+12C	49.24	30.50	S	21.33	29.10	S	13.46	23.67	
	IMPT+IMPT	37.10	31.76	S	20.76	32.91		13.71	27.42	
	12C+12C	35.34	34.17	S	21.72	33.84		14.46	26.39	
Optical Nerve i	IMXT+IMXT	96.08	12.40		89.45	31.45		80.67	29.68	
	IMXT+IMPT	94.80	30.10		88.664	31.296		77.925	30.028	
	IMXT+12C	94.41	17.67		87.57	31.08		74.63	30.91	
	IMPT+IMPT	93.93	18.88		86.54	25.57		75.37	30.29	
	12C+12C	86.22	25.82		78.30	31.10	S	70.94	32.01	
Chiasm	IMXT+IMXT	91.62	25.80		82.93	34.37		64.30	43.77	
	IMXT+IMPT	94.37	16.43		82.831	33.297		63.495	42.342	
	IMXT+12C	95.00	13.13		83.17	33.40		64.66	42.21	
	IMPT+IMPT	88.05	18.16		72.15	37.86		61.28	41.18	
	12C+12C	80.38	31.23		71.01	40.08		63.84	39.82	
Hypophysis	IMXT+IMXT	100.00	0.00		98.12	4.16		82.22	27.98	
	IMXT+IMPT	100.00	0.00		98.93	2.13		85.60	21.56	
	IMXT+12C	100.00	0.00		98.34	3.32		83.89	23.67	
	IMPT+IMPT	100.00	0.00		99.95	0.15		92.41	13.03	
	12C+12C	99.32	2.04		95.02	9.97		85.59	26.47	

TABLE 5.2: Averaged dosimetric parameters $V_{20\%}$, $V_{50\%}$, $V_{80\%}$ for selected primary OAR and the significant differences (depicted by S)

		D 2% [Gy(RBE)]		p	D 50% [Gy(RBE)]		p	D mean [Gy(RBE)]		p
		Mean value	Standard deviation		Mean value	Standard deviation		Mean value	Standard deviation	
Brain c	IMXT+IMXT	51.37	15.34		6.25	3.89		11.84	4.76	
	IMPT+IMPT	33.02	23.28	S	0.13	0.03	S	2.14	1.59	S
	12C+12C	30.32	22.55	S	0.25	0.19	S	2.30	1.66	S
Brain i	IMXT+IMXT	68.47	6.16		32.45	13.63		32.18	9.70	
	IMPT+IMPT	65.07	10.09	S	5.64	4.85	S	15.59	6.46	S
	12C+12C	61.15	20.65		4.07	3.66	S	13.22	6.29	S
Cochlea c	IMXT+IMXT	24.39	6.91		23.26	6.57		23.11	6.65	
	IMPT+IMPT	0.85	1.50	S	0.73	1.19	S	0.65	1.14	S
	12C+12C	3.42	3.65	S	2.60	2.50	S	2.59	2.65	S
Cochlea i	IMXT+IMXT	59.59	21.26		57.85	21.29		57.80	21.25	
	IMPT+IMPT	59.99	21.24		58.58	21.01		58.47	20.98	
	12C+12C	57.34	21.22		54.47	21.05		54.26	20.90	
Hippo c	IMXT+IMXT	33.24	16.87		17.14	6.17		18.03	7.61	
	IMPT+IMPT	14.74	22.26	S	1.61	2.91	S	3.24	5.81	S
	12C+12C	17.63	23.39	S	2.72	3.15	S	4.48	5.87	S
Hippo i	IMXT+IMXT	68.75	2.34		54.05	13.57		53.39	12.31	
	IMPT+IMPT	65.89	3.79		45.18	22.63		45.15	19.64	
	12C+12C	64.48	5.91		40.39	26.00	S	41.28	21.42	S
Hypoth c	IMXT+IMXT	49.34	17.72		42.87	16.15		42.56	16.05	
	IMPT+IMPT	35.55	24.63	S	24.58	22.05	S	25.24	21.68	S
	12C+12C	35.24	25.72	S	22.84	23.05	S	23.78	22.36	S
Hypoth i	IMXT+IMXT	57.47	14.06		51.43	12.42		51.38	12.31	
	IMPT+IMPT	52.75	19.31		44.10	20.71		43.97	20.01	
	12C+12C	51.08	21.98		38.90	23.06	S	39.36	21.82	S

TABLE 5.3: Averaged dosimetric parameters $D_{2\%}$, $D_{50\%}$, D_{mean} for selected secondary OAR and the significant differences (depicted by S)

		V 20% [%]		p	V 50% [%]		p	V 80% [%]		p
		Mean value	Standard deviation		Mean value	Standard deviation		Mean value	Standard deviation	
Brain c	IMXT+IMXT	28.40	12.30		6.25	3.89		2.92	2.96	
	IMPT+IMPT	4.24	23.28	S	0.13	0.03	S	1.10	1.14	S
	12C+12C	3.57	2.97	S	1.89	1.75	S	1.06	1.06	S
Brain i	IMXT+IMXT	67.84	16.83		48.10	19.82		22.72	11.51	
	IMPT+IMPT	31.10	13.09	S	19.11	8.47	S	12.92	6.53	S
	12C+12C	23.35	11.28	S	15.70	8.42	S	11.00	6.58	S
Cochlea c	IMXT+IMXT	90.00	31.62		0.00	0.00		0.00	0.00	
	IMPT+IMPT	0.00	0.00	S	0.00	0.00		0.00	0.00	
	12C+12C	0.00	0.00	S	0.00	0.00		0.00	0.00	
Cochlea i	IMXT+IMXT	90.00	31.62		90.00	31.62		75.81	42.04	
	IMPT+IMPT	90.00	31.62		90.00	31.62		85.56	33.15	
	12C+12C	90.00	31.62		88.97	31.43		61.36	49.39	
Hippo c	IMXT+IMXT	68.09	27.66		7.04	14.06		1.81	3.92	
	IMPT+IMPT	7.14	15.21	S	2.91	6.62		0.78	2.18	
	12C+12C	7.61	15.32	S	2.77	5.95		0.99	2.27	
Hippo i	IMXT+IMXT	95.65	8.80		84.28	20.44		60.37	30.91	
	IMPT+IMPT	81.55	20.85	S	68.42	30.90		51.72	40.12	
	12C+12C	75.32	27.34	S	63.50	35.01	S	46.09	39.29	
Hypoth c	IMXT+IMXT	99.73	0.84		72.49	40.85		31.37	43.88	
	IMPT+IMPT	53.14	47.44	S	30.18	40.43	S	18.11	35.15	
	12C+12C	42.48	44.39	S	31.63	44.95	S	19.33	36.91	
Hypoth i	IMXT+IMXT	100.00	0.00		90.00	31.62		44.37	37.11	
	IMPT+IMPT	93.95	13.41		66.57	44.34		43.28	43.89	
	12C+12C	74.27	43.03		57.51	42.82	S	37.94	42.53	

TABLE 5.4: Averaged dosimetric parameters $V_{20\%}$, $V_{50\%}$, $V_{80\%}$ for selected secondary OAR and the significant differences (depicted by S)

Bibliography

- [1] W. Röntgen, “Über eine neue art von strahlen. vorläufige mitteilung,” *Sitzungsberichte der physikalisch-medizinischen Gesellschaft zu Würzburg*, vol. Sitzung 30, pp. 132–141, 1895.
- [2] H. Krieger and W. Petzold, *Strahlenphysik, Dosimetrie und Strahlenschutz I.: Grundlagen*. Strahlenphysik, Dosimetrie und Strahlenschutz / von Hanno Krieger und Wolfgang Petzold, Teubner B.G. GmbH, 1992.
- [3] A. Becquerel, “Sur les radiation émises par phosphorescence,” *Compt.Rend.Acad.Sci*, vol. 122, pp. 420–421, 1896.
- [4] P. Curie and M. Curie, “Sur une substance nouvelle radioactive, contenue dans la pechblende,” *Compt.Rend.Acad.Sci*, vol. 127, p. 175, 1898.
- [5] H. Kogelnik, “Inauguration of radiotherapy as a new scientific speciality by leopold freund 100 years ago,” *Phys Med Biol*, vol. 45, pp. 1229–1241, 2010.
- [6] H. Kaplan, “Basic principles in radiation oncology,” *Cancer*, vol. 39, pp. 689–693, 1977.
- [7] A. Becquerel and P. Curie, “Action physiologique des rayons de radium,” *Compt.Rend.Acad.Sci*, vol. 132, pp. 1289–1291, 1901.
- [8] C. Beck, *Roentgen ray diagnosis and therapy*. Appelton, 1904.
- [9] L. Freund, *Elements of general radiotherapy for practitioners*. Rehman, 1904.
- [10] C. Regaud and R. Ferroux, “Discordance des effets de rayons x. d’une part dans la peau, d’autre part dans le testicule, par le fractionnement de la dose,” *Compt.Rend.Soc.Biol.*, vol. 97, pp. 431–434, 1927.
- [11] H. Coutard, “Principles of x-ray therapy of malignant disease,” *Lancet*, vol. 2, pp. 1–12, 1934.

- [12] W. Coolidge, "Cathode-ray and roentgen-ray work in progress," *Am.J.Roentgenol.*, vol. 19, pp. 313–321, 1928.
- [13] C. Karzmark, "Electron linear accelerators for radiation therapy: history, principles and contemporary developments," *Phys Med Biol*, vol. 18, pp. 321–354, 1973.
- [14] P. Mayles, A. Nahum, and J. Rosenwald, *Handbook of radiotherapy physics - Theory and Praxis 1*. Taylor and Francis Group, 2007.
- [15] B. Vujosevic, "Radiotherapy: past and present," *Arch Onco*, vol. 18(4), pp. 140–142, 2010.
- [16] J. Campbell, *Website on Lord Ernest Rutherford, including a comprehensive bibliography*. <http://www.rutherford.org.nz/bibliography.htm>, 2010.
- [17] E. Courant, "Early milestones in the evolution of accelerators," *Reviews of accelerator science and technology*, vol. 1, pp. 1–5, 2008.
- [18] R. Graaff, "A 1 500 000 volt electrostatic generator," *Phys.Rev.*, vol. 38, p. 0, 1919.
- [19] J. Cockcroft, "Experiments with high velocity positive ions," *Proc.R.Soc.Lond.*, vol. 129, pp. 477–489, 1930.
- [20] E. Lawrence and M. Livingston, "The production of high speed light ions without the use of high voltage," *Phys.Rev.*, vol. 40, pp. 19–35, 1932.
- [21] E. McMillan, "The origin of the synchrotron," *Phys.Rev.*, vol. 69, p. 543, 1946.
- [22] K. Bethge, G. Walter, and B. Wiedemann, *Kernphysik*. Springer Verlag, 2001.
- [23] W. Demtröder, *Experimantalphysik 4*. Springer Verlag, 1998.
- [24] U. Linz, *Ion beam therapy*. Springer Verlag, 2012.
- [25] R. Wilson, "Radiological use of fast protons," *Radiology*, vol. 47, pp. 487–491, 1946.
- [26] C. Greco and S. Wolden, "Current status of radiotherapy with proton and light ion beams," *Cancer*, vol. 109, pp. 1227–1238, 2007.
- [27] G. Kraft, "Tumor therapy with heavy charged particles," *Prog Part Nucl Phys*, vol. 45, p. 473–544, 2000.
- [28] D. Miller, "A review of proton beam radiation therapy," *Med.Phys.*, vol. 22, pp. 1943–1954, 1995.
- [29] C. Tobias and J. Lawrence, "Pituitary irradiation with high-energy proton beams a preliminary report," *Cancer Res.*, vol. 18, p. 121, 1958.

- [30] B. Larsson and L. Leksell, "The high-energy proton beam as a neurosurgical tool," *Nature*, vol. 182, p. 1222, 1958.
- [31] J. Slater and D. Miller, "Development of a hospital-based proton beam treatment center," *Int. J. Radiat. Oncol. Biol. Phys.*, vol. 14, p. 761, 1988.
- [32] J. Castro and D. Linstadt, "Experience in charged particle irradiation of tumors of the skull base: 1977-1992," *Int. J. Radiat. Oncol. Biol. Phys.*, vol. 29, pp. 647-655, 1994.
- [33] J. Castro, "Results of heavy ion radiotherapy," *Radiat. Environ. Bio-phys.*, vol. 34, pp. 45-48, 1995.
- [34] F. M. Khan, *The physics of radiation therapy*. Lippincott Williams & Wilkins, 3 ed., 2003.
- [35] M. Krämer, W. Weyrather, and M. Scholz, "The increased biological effectiveness of heavy charged particles: from radiobiology to treatment planning," *Techn. Cancer Res. Treatm.*, vol. 2, pp. 427-436, 2003.
- [36] H. Paganetti, "Interpretation of proton relative biological effectiveness using lesion induction, lesion repair, and cellular dose distribution," *Med. Phys.*, vol. 32, p. 2548-2556, 2005.
- [37] T. Kanai, N. Matsufuji, and T. Miyamoto, "Examination of the system for HIMAC carbon therapy," *Int J Radiat Oncol Biol Phys.*, vol. 64, pp. 650-656, 2006.
- [38] I. R. 50, *Prescribing, Recording and Reporting Photon Beam Therapy*. International Commission on Radiation Units and Measurements, 1993.
- [39] E. Hall, "Intensity-modulated radiation therapy, protons, and the risk of second cancers," *Int J Radiat Oncol Biol Phys.*, vol. 65, pp. 1-7, 2006.
- [40] M. Brada, M. Johannesma, and D. Ruyscher, "Proton therapy in clinical practice: Current clinical evidence," *J Clin Oncol*, vol. 25, pp. 965-970, 2007.
- [41] M. Hillbrand and D. Georg, "Assessing a set of optimal user interface parameters for intensity-modulated proton therapy planning," *Med. Phys.*, vol. 11, pp. 93-104, 2010.
- [42] A. Bielajew, *Fundamentals of the Monte Carlo method for neutral and charged particle transport*. <http://www-personal.engin.umich.edu/~bielajew/MCBook/book.pdf>, 2001.
- [43] W. Press and S. Teukolsky, *Numerical Recipes in C++*. Cambridge UP GB, 2002.

- [44] T. Bortfeld, “Optimized planning using physical objectives and constraints,” *Semin Radiat Oncol*, vol. 9, p. 20–34, 1999.
- [45] A. Brahme, “Optimized radiation therapy based on radiobiological objectives,” *Semin Radiat Oncol*, vol. 9, p. 35–47, 1999.
- [46] I. 83, *Prescribing, recording and reporting intensity-modulated-photon beam Therapy (IMRT)*. The International Commission on Radiation Units and Measurements., 2010.
- [47] K. Jothybasu, A. Bahl, and V. Subramani, “Static versus dynamic intensity-modulated radiotherapy: Profile of integral dose in carcinoma of the nasopharynx,” *J Med Phys*, vol. 34(2), p. 66–72, 2009.
- [48] A. Lomax, “Intensity modulated methods for proton therapy,” *Phys Med Biol*, vol. 44, pp. 185–205, 1999.
- [49] F. Albertini, “Is it necessary to plan with safety margins for actively scanned proton therapy,” *Phys Med Biol*, vol. 56, pp. 4399–4413, 2011.
- [50] D. Louis, “The 2007 who classification of tumours of the central nervous system,” *Acta Neuropathol*, vol. 114, pp. 97–109, 2007.
- [51] L. Palma, “Long-term prognosis for atypical and malignant meningiomas: a study of 71 surgical cases,” *Neurosurg Focus*, vol. 2, p. e3, 1997.
- [52] M. Kallio, “Factors affecting operative and excess long-term mortality in 935 patients with intracranial meningioma,” *Neurosurgery*, vol. 31, pp. 2–12, 1992.
- [53] S. Combs, “Treatment of patients with atypical meningiomas simpson grade 4 and 5 with a carbon ion boost in combination with postoperative photon radiotherapy: The marcie trial,” *BMC Cancer*, vol. 10, pp. 615–623, 2010.
- [54] O. Salazar, “Ensuring local control in meningiomas,” *Int J Radiat Oncol Biol Phys*, vol. 15, pp. 501–504, 1988.
- [55] E. Lusi and D. Gutmann, “Meningioma: an update,” *Curr Opin Neurol*, vol. 17, pp. 687–692, 2004.
- [56] S. Milker-Zabel, “Fractionated stereotactic radiotherapy in patients with benign or atypical intracranial meningioma: long-term experience and prognostic factors,” *Int J Radiat Oncol Biol Phys*, vol. 61, pp. 809–816, 2005.
- [57] R. Komotar, J. Iorgulescu, and D. Raper, “The role of radiotherapy following gross total resection of atypical meningiomas,” *J Neurosurg*, vol. 117(4), pp. 679–686, 2012.

- [58] S. Adeberg, C. Hartmann, and T. Welzel, “Long-term outcome after radiotherapy in patients with atypical and malignant gliomas – clinical results in 85 patients treated in a single institution leading to optimized guidelines for early radiation therapy,” *Int J Radiat Oncol Biol Phys*, vol. 83(3), pp. 859–864, 2012.
- [59] I. R. 78, *Prescribing Recording and Reporting Proton-Beam Therapy*. International Commission on Radiation Units and Measurements, 2007.
- [60] M. Alber and F. Nusslin, “An objective function for radiation treatment optimization based on local biological measures,” *Phys Med Biol*, vol. 44, pp. 479–493, 1999.
- [61] M. Fippel, “Fast monte carlo dose calculation for photon beams based on the vmc electron algorithm,” *Med Phys*, vol. 26, pp. 1466–1475, 1999.
- [62] A. Niemierko, “Reporting and analyzing dose distributions: A concept of equivalent uniform dose,” *Med Phys*, vol. 24, pp. 103–110, 1997.
- [63] E. CMS, *Monaco Training Guide v.2.04*. LTGMON0204, 2010.
- [64] M. Soukup and M. Fippel, “A pencil beam algorithm for intensity modulated proton therapy derived from monte carlo simulations,” *Phys. Med. Biol*, vol. 50, p. 5089–5104, 2005.
- [65] B. Reitz and M. Miften, “Comparison of the konrad imrt and xio treatment planning systems,” *J O APPL CLIN MED PHYS*, vol. 9, pp. 122–135, 2008.
- [66] M. Kraemer, O. Jaekel, and T. Haberer, “Treatment planning for heavy-ion radiotherapy: physical beam model and dose optimization,” *Phys Med Biol*, vol. 45(11), p. 3299–3317, 2000.
- [67] M. Kraemer and M. Scholz, “Treatment planning for heavy-ion radiotherapy: calculation and optimization of biologically effective dose,” *Phys Med Biol*, vol. 45(11), p. 3319–3330, 2000.
- [68] O. Jaekel, M. Kraemer, C. Karger, and J. Debus, “Treatment planning for heavy ion radiotherapy: clinical implementation and application,” *Phys Med Biol*, vol. 46(4), p. 1101, 2001.
- [69] M. Scholz and G. Kraft, “Track structure and the calculation of biological effects of heavy charged particles,” *Adv Space Res*, vol. 18(1-2), p. 5–14, 1996.
- [70] M. Scholz, A. Kellerer, W. Kraft, and G. Kraft, “Computation of cell survival in heavy ion beams for therapy: The model and its approximation,” *Radiat Environ Biophys*, vol. 36(1), p. 59–66, 1997.

- [71] S. Minohara, T. Kanai, M. Endo, and K. Kawachi, "Effects of object size on a function to convert x-ray ct numbers into the water equivalent path length of charged particle beam," *Proc. of the Third Workshop on Physical and Biological Research with Heavy Ions*, vol. 1, p. 14–15, 1993.
- [72] C. Jacob, "Reichweite-ct-zahl-beziehung von phantommateriellen und messungen mit einer neuentwickelten mulitsegmentierten ionisationskammer zur dosisverifikation bei schwerionenbestrahlung," *PhD thesis*, vol. 1, p. 1–100, 1996.
- [73] O. Geiss, D. Schardt, B. Voss, M. Krämer, and G. Kraft, "Correlation between ct number and water equivalent thickness," *Technical report*, vol. 1, pp. 94–109, 1999.
- [74] CERR, *Website about CERR*. <http://www.cerr.info>, 2003.
- [75] I. Paddick, "A simple scoring ratio to index the conformity of radiosurgical treatment plans," *J Neurosurg*, vol. 93, p. 219–222, 2000.
- [76] L. Papula, *Mathematische Formelsammlung*. vieweg, 1986.
- [77] K. Kosaki, S. Ecker, and D. Habermehl, "Comparison of intensity modulated radiotherapy (imrt) with intensity modulated particle therapy (impt) using fixed beams or an ion gantry for the treatment of patients with skull base meningiomas," *Radiat Oncol*, vol. 22, p. 7:44, 2012.
- [78] E. Dennis, M. Bussiere, and A. Niemierko, "A comparison of critical structure dose and toxicity risks in patients with low grade gliomas treated with imrt versus proton radiation therapy," *Technol Cancer Res Treat*, vol. 12(1), pp. 1–9, 2013.
- [79] L. Feuvret, G. Noel, and D. Weber, "A treatment planning comparison of combined photon-proton beams versus proton beams-only for the treatment of skull base tumors," *Int J Radiat Oncol Biol Phys*, vol. 63(3), pp. 944–954, 2007.
- [80] F. Paulsen and D. Zips, "Radiation therapy of meningioma of the anterior visual pathway," *Ophthalmologie*, vol. 110(5), pp. 427–432, 2013.
- [81] S. Combs, C. Hartmann, and A. Nikoghosyan, "Carbon ion radiation therapy for high-risk meningiomas," *Radiotherapy and Oncology*, vol. 95, p. 54–59, 2010.
- [82] D. Schulz and H. Tsujii, "Particle radiation therapy using proton and heavier ion beams," *J Clin Oncol*, vol. 25, p. 953–964, 2007.
- [83] D. Schulz, C. Karger, and A. Feuerhake, "Effectiveness of carbon ion radiotherapy in the treatment of skull-base chordomas," *Int J Radiat Oncol Biol Phys*, vol. 68, p. 449–457, 2007.

- [84] L. Cozzi, A. Fogliata, and A. Lomax, “A treatment planning comparison of 3d conformal therapy, intensity modulated photon therapy and proton therapy for treatment of advanced head and neck tumours,” *Radiother Oncol*, vol. 61, p. 287–297, 2001.
- [85] R. Feltz and U. Schalldach, “Malignant brain tumors after radiation – glioblastomas after operation and radiation of meningiomas,” *Neurochir*, vol. 62, p. 48–56, 2001.
- [86] O. Jaekel and J. Debus, “Selection of beam angles for radiatiotherapy of skull based tumours using charged particles,” *Phys Med Biol*, vol. 45, pp. 1229–1241, 2000.

List of Figures

1	Comparison of the depth dose distribution of photons, protons and carbon ions as a function of the penetration depth	7
1.1	Coherent scattering ([2],p.120)	12
1.2	Absorption Edges([2],p.108)	13
1.3	Emission of electrons([2],p.109)	14
1.4	Photoelectric effect ([2],p.107)	14
1.5	Compton effect ([2],p.112)	15
1.6	Compton photon ([2],p.112)	15
1.7	Ranges of dominance of various interaction processes ([2],p.125)	19
1.8	Energy losses and amount of particles N as a function of the penetration depth([2],p.191)	20
1.9	Relative biological effectiveness for carbon ions and protons [35]	21
1.10	Straggling effect of various ions ([24],p.49)	23
1.11	Dose deposition as a function of the penetration depth of protons and carbon ions	23
1.12	Various treatment volumes	25
1.13	Cumulative DVH of a planning target volume	26
1.14	Setup of a LINAC ([34],p.43	27
1.15	Drift tube arrangement of a LINAC [22],p.163	28
1.16	Set-up of a synchrotron	30
1.17	Arrangement of a synchrotron in conjunction with LINAC and treatment areas ([24],p.335)	31
1.18	Principle of passive scattering and active scanning proton beam delivery [39]	32
1.19	Comparison of forward planning and inverse planning [46]	38
2.1	Graphical depiction of the target volumes	43
2.2	Delineation of PTV, GTV and OAR	44
2.3	Influence of the k- parameter on the DVH of a serial organ[63]	49
2.4	Influence on the DVH of a parallel organ[63]	50
2.5	Beam directions for $PTV_{initial}$ and PTV_{boost}	52
2.6	Definitions of gantry (g) and couch (c) angles for proton and carbon ion therapy in the present study	55
2.7	Display of the CERR environment	56
3.1	Dose distribution of PTV_{init}	64
3.2	Dose distribution of PTV_{boost}	64
3.3	DVHs of PTVs	64

3.4	DVH of the combined plans	67
3.5	Dose distribution of combined plans	67
3.6	DVHs of eyes	69
3.7	DVHs of optical nerves	70
3.8	DVH of chiasm	71
3.9	DVHs of brainstem and cerebellum	72
3.10	DVH of hypophysis	73
3.11	Comparison of sole and mixed treatment combinations for various primary OARs	74
3.12	DVH of brain hemispheres	75
3.13	DVH of cochlea _c , hippocampus _c and hypothalamus _c	76
3.14	DVH of cochlea _i , hippocampus _i and hypothalamus _i	77
4.1	Progression-free survival curve [81]	81

Curriculum Vitae

Personal Information

Name: Lukas Soelkner
Date of Birth: 16.12.1986, Waidhofen/Ybbs, Austria
Adress: Glatzgasse 4/24
1190 Wien
Telephone: 0676/3423877

Education

School

1993 - 1997 Elementary school: Zell, Waidhofen/Ybbs
1997 - 2001 Grammar school: Bundesrealgymnasium, Waidhofen/Ybbs
2001 - 2006 Vocational school: Höhere technische Bundeslehranstalt,
Waidhofen/Ybbs (Focus: Engineering management)
school leaving examination (Abitur): June 2006

Study

2007 - 2011 Bachelor programme Technical Physics, Vienna University
of Technology
2011 - 2013 Master programme Biomedical Engineering, Vienna Univer-
sity of Technology
October 2012 - September 2013 Diplomathesis: Comparison of photon, proton and carbon
ion therapy for meningioma patients
AKH Vienna

Work Experience

March-August 2007 Boehler Uddeholm, Boehlerwerk
2009-2012 Tutor, Vienna University of Technology

Skills

Foreign languages: English, Italian (basic), Spanish(basic)